UNIVERSITY OF LEEDS

A dynamic light scattering study of the structural relaxations and dynamics of Poly(N-acetamido acrylamide) (PAAA) thermoreversible hydrogels

Henry Thomas Anthony Pickersgill

PHYS5014M - Final Report

Supervisor: Dr. Johan Mattsson

University of Leeds

School of Physics and Astronomy

Submitted in partial fulfilment of the requirements for the degree of

Bachelor of Science, Master of Physics

April, 2021

Contents

1 Abstract

Dynamic light scattering (DLS) studies have been performed to investigate the properties of gelation and the sol-gel transition, measuring the fluctuations in intensity of scattered light to model the dynamics occurring within a gel. Studies of Poly(N-acetamido acrylamide) (PAAA) hydrogels and stretched exponential fitting to autocorrelation functions provide estimates for β and τ, the stretching parameters and characteristic relaxation times respectively. Other fitting procedures including the use of power-law decays were attempted with less success. The fastest relaxations are shown to be diffusive, where the average decay rate, $\bar{\Gamma}$, scales with q^2 for scattering wave vector q, agreeing with previous studies of a range of systems. The slower relaxations are more complex, with $\bar{\Gamma}$ found to depend on q^γ for γ in the range $0.5 - 6$. The diffusion coefficients are estimated to be of the order $10^{-10}\mathrm{m}^2/\mathrm{s}$, predicting a decrease in the size of gel networks ($\sim \mathrm{nm}$) with increasing solution viscosity and temperature. β for the slow relaxation is observed to critically decrease as τ diverges towards the sol-gel transition temperature. The gelation transitions are studied and critical temperatures estimated for temperature-varying DLS measurements, modelling the sol-gel transition as a weak glass transition. Critical temperatures are also estimated from monitoring the switch between ergodic and non-ergodic regimes. T_c is shown to vary linearly with concentration, c.

2 Introduction

2.1 Gels and gel models

Soft matter physics considers a wide range of materials whose properties and behaviour are easily influenced by thermal fluctuations, including polymers, colloids, glasses, liquid crystals, gels and more [1]. Properties such as structural relaxation times and physical size of soft matter span a large range of orders of magnitude. Structures can exist on mesoscopic length scales, anywhere between the sizes of atoms and molecules to the sizes of macroscopic objects [1]. This study considers polymer gels, formed from a sufficiently dilute three-dimensional network of polymer cross-links, which may be physical (intermolecular: Hydrogen bonding, Van der Waals' forces, electrostatic forces) or chemical cross-links (intramolecular: covalent bonding) [2]. The cross-linking interaction energy $> kT$ for chemical gels and $\sim kT$ for physical gels, reflecting the differing attraction strengths between chemical bonds and intermolecular forces [3]. Chemical gels are thus more suitable for applications requiring long-lasting and irreversible elastic behaviour, such as epoxy resins [4]. The association of polymers in solution causes them to swell, retaining the solution within gel networks. *Hydrogels* form when the swelling agent is water, making them particularly useful for bio-compatible applications, including targeted drug delivery [5] and spinal cord repair [6]. Hydrogels have seen a range of other applications, such as gelling agents in food [7] and optical biosensors [8]. At suitable temperatures and concentrations, polymer networks can be formed across the whole system, forming a continuous material of large molecular mass, behaving elastically when deformed slowly and weakly [9]. The gelation point is thus defined as the point at which the polymer solution can no longer flow freely like a liquid, and its viscosity and structural relaxation times diverge [10].

Gels can be modelled as inter-connected networks of cross-links spanning the entire system [10,11], such as in the statistical percolation model, predicting how sites in a lattice are connected, the sol-gel transition being defined as the point at which all lattice sites are connected by a single path [11,12]. Percolation theory is typically divided into bond-percolation and site-percolation, the former being used in the case where all sites are occupied and bonds must be made, the latter being used in the case where bonds will always be formed if neighbouring lattice sites are occupied. Both these models in tandem can predict upper and lower bounds for the concentration of polymer in solution at which gelation occurs (i.e. when the network is spanned

fully by paths of connections). This is demonstrated in figure 2.1.1.

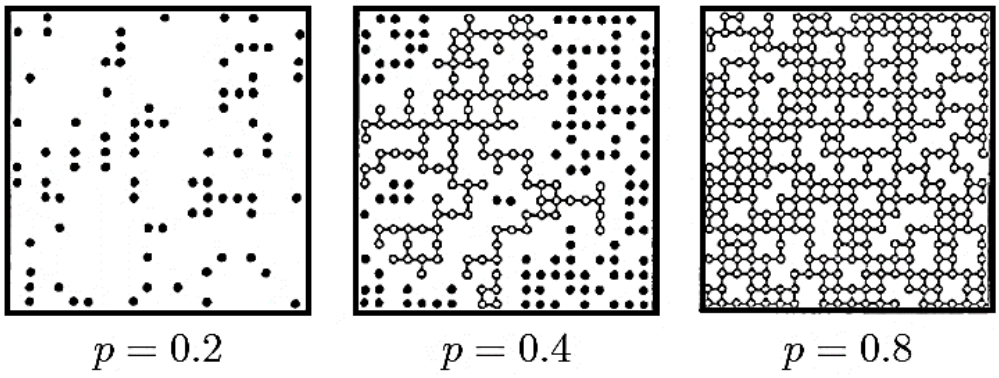

Figure 2.1.1. Percolation networks for three values of p; the probability that a site is occupied. The filled circles correspond to local clusters, while the hollow circles represent a cluster which spans the entire network. $p = 0.2$ is a representation of the sol state, where minimal strong cross-links have been made. For $p = 0.4$, networks begin to form, but the whole system is not yet spanned by all polymer cross-links. For $p = 0.8$, the system is spanned completely by all cross-links i.e. the gel phase [13].

In addition to this, polymers are fractal – appearing self-similar at a range of length scales. The fractal nature of polymers gives rise to a power-law relationship between the polymer chain size and molecular mass: $M \sim R^{d_f}$ where d_f is the fractal dimension of the polymer, characterising the way in which a shape/object fills space [10]. For compact 3D spheres, $d_f \approx 3$, reflecting the way in which the volume is filled. Thus, one could expect a change in the fractal dimension of the polymer (ideal polymer chains have $d_f = 2$) when approaching the gel phase [14], because the higher the fractal dimension, the more compact the gel clusters are within solution [10,15]. For the polymer (PAAA) studied in this research, Marstokk et. al. (1998) have demonstrated an increase in d_f with polymer concentration. The combination of the fractal nature of gels and percolation models gives rise to power-law relationships between various measurable quantities, such as structural relaxation times, diffusion coefficients, concentration, and elastic moduli [16]. For example, the stress relaxation modulus is found to vary with the frequency of the applied stress according to a power-law [17].

The gelation phase is generally investigated using rheological and microrheological tests; studies of the flow and elastic responses of a material [3,17,18]. In stress relaxation studies, Newtonian liquids and solids respond to applied stresses in a predictable manner, constant strain rate and constant strain respectively. Highly concentrated polymers (melts) and polymer solutions (sol) are defined as viscoelastic liquids, simultaneously comprised of viscous (liquid-like) and elastic (solid-like) properties; both behaviours are both observed in stress relaxation studies. A characteristic feature of viscoelastic materials is the terminal relaxation, an eventual decline in the stress relaxation modulus to zero [19]. This is not observed in systems formed from networks of cross-links, as gels are defined by their ability to respond elastically, even over long periods of time. Gels are therefore more closely related to viscoelastic solids; whose stress relaxation modulus also reaches a finite plateau [19,20]. This is generally substantial criteria for the classification of a gel, although other studies can be performed to confirm this, for example, using x-ray, neutron, or visible light scattering [21].

Polymer chains can be described by many models, such as the Rouse, Zimm and reptation models, although other models do exist [22,23,24]. The Rouse model treats polymer chains as a network of masses connected by elastic springs, with the relaxation times of the network modelled by the fundamental vibrational modes excited along the chain. Hydrodynamic interactions, interactions between polymer chains and the solution, are neglected [10,25]. This model is much more applicable to high concentration polymers and polymer melts. In contrast, the Zimm model considers cooperative motion of polymer and solution when

hydrodynamic interactions are significant, used to model dilute and semi-dilute polymer solutions [22]. A common approximation to both these models is the effect of excluded volume, the net effect of attractive and repulsive interactions between monomers, are discarded in both cases [26]. For long decay times, the reptation model can be applied, describing the motions of polymer chains in entangled systems through a surrounding tube (a region of space where the chain lies, formed from repulsion due to steric hindrance of neighbouring chains) [19,25].

The motions of polymer chains are thus quantified using the relaxation time, $\tau \sim$ the time taken for polymer chains to diffuse their own size in the case of simple diffusion (Brownian motion) [21,27]. At small enough time scales, relaxations observed are well described by cooperative diffusion of polymer chains, as timescales are not long enough to promote other interactions [25,28]. At larger time scales, relaxations are significantly more complex, the origins of such relaxations not universally agreed upon. Wang et. al. (1992) attribute these slower relaxations to viscoelastic effects, whereas Svanberg et. al. (1999) treat them as analogous to the α-relaxation in a glassy system (the relaxation resulting in the glass transition). The characteristic structural relaxation times of polymers differ between the Rouse, Zimm and reptation models – measurements of τ in a polymer system can reveal the most applicable model.

2.2 Poly(N-acetamido acrylamide) systems

This research considers the properties of association in water for the polymer PAAA, formed from monomers as depicted in figure 2.2.1.

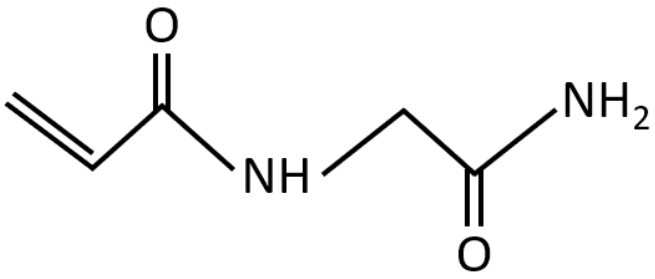

Figure 2.2.1 Chemical structure of the repeating unit within the amphiphilic Poly(N-acetamido acrylamide) (PAAA) polymer used in this study [10,29].

PAAA monomers are *amphiphilic*, formed from electropositive/hydrophobic (Carbon and Hydrogen) and electronegative/hydrophilic (Oxygen and Nitrogen) sections. This gives rise to strong Hydrogen bonding to polar water molecules as well as to neighbouring polymer chains. Thus, strong associations are made when the polymer is dissolved in water, forming physical links between chains and, in the right conditions, a gel. Hydrogels can also be formed from purely hydrophilic polymers, however, as the same association to water is present. Physical gels can be classified as strong or weak, dependent on their resistance to reversible phase transitions [28,29]. PAAA systems have previously been investigated by Marstokk et. al. (1998) and Ostrovskii et. al. (1999) and are thought to form weak, *thermoreversible* hydrogels, where the gelation transition can be reversed through an opposing change in temperature [29]. PAAA is thought to exist in its gel state at room temperature [10,29]. Dynamic light scattering experiments were performed and analysed in this research to determine the properties of PAAA gel systems of various concentrations and under a range of environmental conditions.

2.3 Studying gels with dynamic light scattering

Scattering is used in many areas of physics to probe microscopic structures and reveal the arrangement of atoms or molecules [21]. Typically performed using a wide range of radiation, such as neutrons, X-rays, visible light and electrons, the choice of radiation depends entirely on the comparability between the wavelength of radiation and the characteristic length scales describing the structures of a system [21]. When light passes through a non-uniform medium containing dispersed particles, electric dipoles are induced in the electron clouds of the atoms of the particles, causing either reflection, refraction, absorption, change in polarisation or scattering of the incident light [21], where the preferred mechanism is entirely dependent on the radiation used and the size of the particles. For polymer gels, typical length scales are of the order 100s of nanometres to microns, thus visible light (average $\sim 500\text{nm}$) is suitable for probing gel structures and dynamics. Therefore, measurements of the motions within a gel, either during the gel phase or during the sol phase, are commonly made using either static or dynamic light scattering. Static light scattering (SLS) is an experimental technique used to measure the intensity of scattered light as a function of the scattering angle. Rayleigh theory predicts the intensity of scattered light is dependent on the size of the particles in the sample, thus, in polymer physics, SLS is commonly used to determine the molecular weight of polymer solutions and gels, in addition to the fractal dimension of the clusters [10]. The research conducted in this project, however, considered the use of dynamic light scattering (DLS), a method concerned with measurement of the *fluctuations* in intensity of light scattering from a sample over time, less frequently used to study gel systems [30]. These fluctuations are a direct result of dynamics and density fluctuations in the sample [21]. DLS can be used to measure structural relaxation times, as well as diffusion coefficients and the sizes of cross-linked networks [2]. Figure 2.3.1 demonstrates the scattering process.

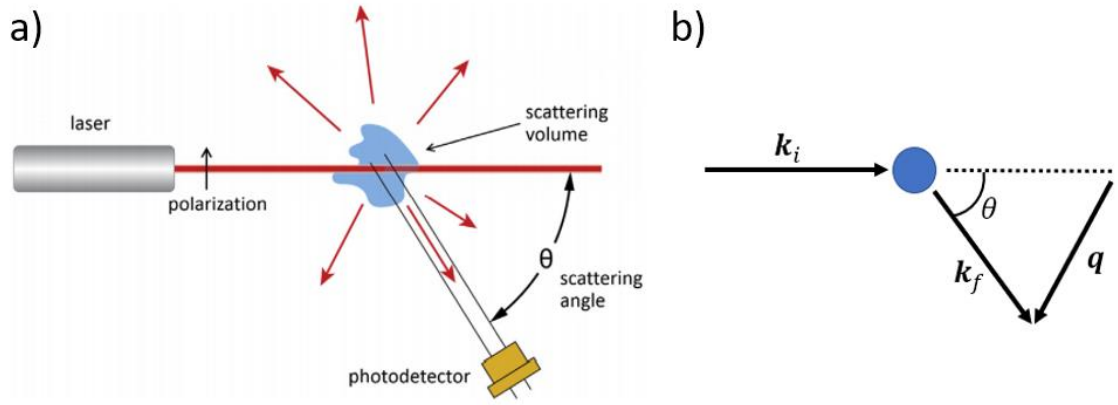

Figure 2.3.1. a) A schematic depiction of a simple scattering experiment. Laser light scatters from a sample and it detected by a photodetector. Detector angles are variable and scattering intensity can be measured as a function of this angle (SLS) or time-fluctuations in the intensity at constant angle can be measured (DLS) [21,31]. b) incoming light undergoes a change of wave vector, $\vec{k}_i$ to $\vec{k}_f$ with difference defined by the scattering wave vector, $\vec{q}$.

The change in wave vector of incoming light to outgoing light is defined as the *scattering wave vector*, q, defined by the geometry shown in figure 2.3.1:

$$q = \frac{4\pi}{\lambda}\sin\left(\frac{\theta}{2}\right) = \frac{4\pi n}{\lambda_0}\sin\left(\frac{\theta}{2}\right), \tag{2.3.1}$$

where λ is the wavelength of light *within* the sample, $\lambda_0 = \lambda/n$ is the laser wavelength in a vacuum, n is the refractive index of the solution and θ is the angular position of the detector. q is important to study, as q^{-1} provides an estimate for the probed length scale [10]. In DLS experiments, the intensity of scattered light is

monitored over time for varying delay/lag times, τ, between measurements [32], typically varied across the microsecond range to 100s of seconds, allowing for a large distribution in the size of traversed paths by the chains before the intensity is measured again. The measured intensities at time t and time $t+\tau$ are compared, determining the correlation between the fluctuations in intensity (how related the measurements are) [10]. The fluctuations within the medium gives rise to a variation in the profile of scattered radiation. In situations where scattered light constructively interferes, a bright spot is seen is seen the sample [2,28]. A time-dependent, irregular 'speckle' pattern is produced, where chosen sections of the pattern are monitored over time. An example of an intensity trace is shown in figure 2.3.2, demonstrating the nature of the irregular speckle pattern.

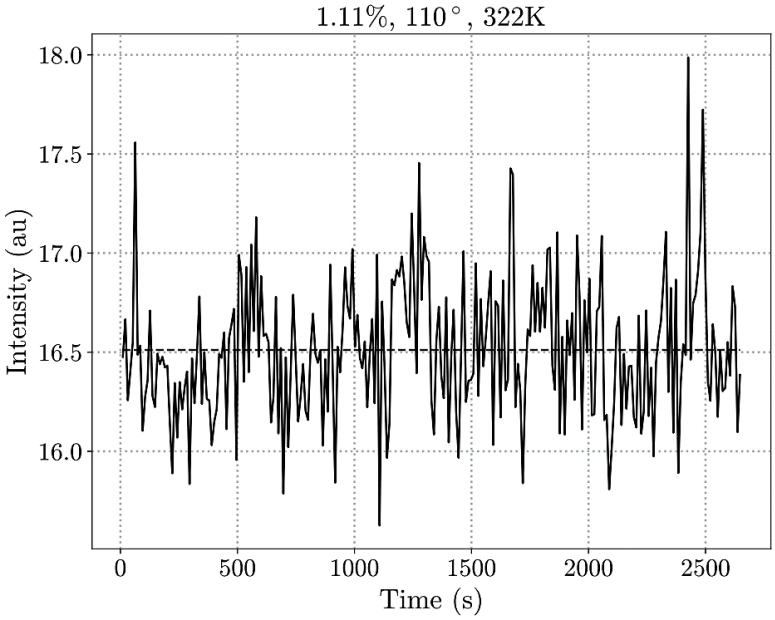

Figure 2.3.2. Intensity variation of a speckle in the pattern over time. The intensity is measured in counts on a photodetector, and peaks (troughs) correspond to bright (dark) spots in the pattern. 1.11wt% sample with $T = 322\text{K}$ and $\theta = 110°$ ($q = 26.7\mu\text{m}^{-1}$).

An auto-digital correlator (ADC) calculates the intensity autocorrelation function [33] (ACF), g_2, defined mathematically as a continuous product of intensities separated by τ taken across a period, P.

$$g_2(\tau) \propto \lim_{P\to\infty} \frac{1}{P}\int_0^P I(t)\cdot I(t+\tau)dt \approx \frac{1}{P}\sum_{i=0}^{P} I(t_i)\cdot I(t_i+\tau) = \langle I(t)\cdot I(t+\tau)\rangle, \tag{2.3.2}$$

where $I(t)$ is the intensity measured at time t. Relabelling $t \to 0$ and $\tau \to t$ to avoid variable conflicts, the intensity ACF, g_2, is defined by normalising equation 2.3.2 by the large lag-time limit ($t \to \infty$), $\langle I(t)\rangle^2$ [2]. In practice however, absolute intensity cannot be measured, as photodetectors are digital, measuring intensities in the form of discrete counts. The calculated ACF is thus an approximation, hence the RHS of equation 2.3.2. Therefore,

$$g_2(t) = \frac{\langle I(0)\cdot I(t)\rangle}{\langle I(t)\rangle^2} \tag{2.3.3}$$

is a dimensionless quantity characterising the correlation between measurements of the count rates $I(t=0)$ and $I(t)$ of a small area point of the speckle pattern [34]. $\langle\cdots\rangle$ denotes a mean average taken over all time [35], and the intensity is related to the electric field $I(t) = |E(t)|^2$ [16,23]. g_2 indicates how relaxations approach equilibrium on the currently probed length scale, given by the choice of q. The scattered intensity at a point can fluctuate between zero and close to $2\cdot\langle I(t)\rangle$, as such, ADCs output the quantity $g_2(t)-1$, ensuring the ACF decays to zero at large t [2]. The intensity ACF is directly measurable, although is indirectly linked to the properties of the sample. Therefore, the electric field ACF, $g_1(t)$ can be studied, as it is directly

related to the Fourier component of the density fluctuations of particles, and electric fields are not directly measurable [23,32]. $g_1(t)$ is defined as:

$$g_1(t) = \frac{\langle E(0) \cdot E(t) \rangle}{\langle E(t) \rangle^2} = \frac{\langle E(0) \cdot E(t) \rangle}{\langle I(t) \rangle}, \tag{2.3.4}$$

where $E(t)$ are the electric field amplitudes measured at lag time t. g_1 provides a closer insight into the dynamics and density fluctuations within the sample, thus may be more useful to study. In the case of simple diffusion (Brownian motion), particles undergo random walks (path taken is chosen at random at each timestep) and g_1 is related to a Gaussian probability distribution of the displacements [18].

$$g_1 \sim \exp\left(\frac{-q^2 \langle \Delta r^2(t) \rangle}{6}\right) \tag{2.3.5}$$

where $\langle \Delta r^2(t) \rangle$ is the ensemble averaged, mean squared displacement across the sample (see appendix 7.1). Equation 2.35 relies on the Stokes-Einstein relation, valid for uniform spheres diffusing through a viscous medium [18]. For gel systems in the sol state, equation 2.3.5 can be used to predict the form of g_1, whereas in the gel state, and for longer relaxation times, the dynamics become significantly more complex [28]. Commonly, more complex dynamics are described using *power laws* or *stretched exponentials* of the forms

$$g_1(t) \sim t^{-\alpha} \tag{2.3.6a}$$

$$g_1(t) \sim e^{-(t/\tau)^{\beta}}. \tag{2.3.6b}$$

Equation 2.3.6a is used in cases where a linear relationship in a log-log plot of g_1 vs t is revealed, α being an empirical parameter. For example, it has been reported in some systems, such as colloidal gel suspensions [36] and PMMA gels [30], the slow relaxation shows power-law behaviour during the gelation phase. Equation 2.3.6b is commonly used to describe glassy systems [14]; β represents the stretching parameter, related to the fractal dimension of the system and the breadth of the decay, and τ represents a characteristic decay time [25]. Through variation of β, the characteristic shape of a decay can be deformed (stretched or compressed), with $\beta = 1$ representing a single exponential decay. This is demonstrated in figure 2.3.3.

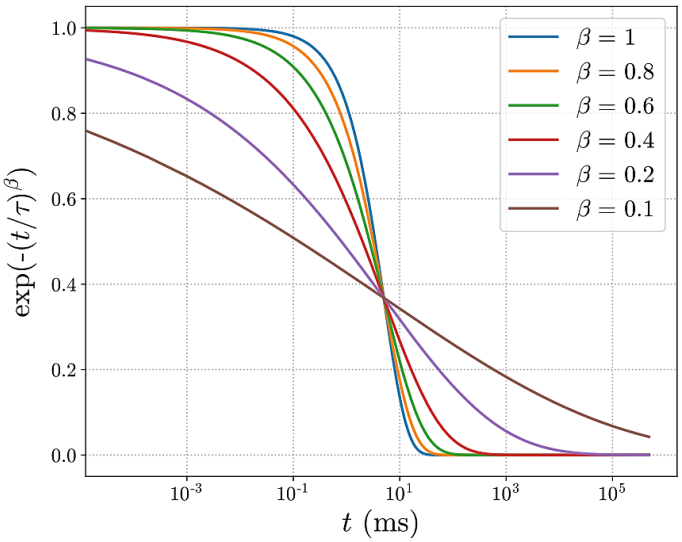

Figure 2.3.3. Simulated stretched exponentials for various stretching parameters between 0 and 1. Notice the broadening of the decay as β is decreased from the single exponential regime, $\beta = 1$. $\tau = 5\text{ms}$ for all curves. The lag time axis is taken from a real set of data.

$\beta < 1$ is indicative of a superposition of single exponentials, all with different decay times (see appendix 7.2), while $1 < \beta < 2$ represents the compressed exponential function, less relevant to polymer physics [37]. It is

thus common to fit g_1 with stretched exponentials as a variety of different dynamics in the gel are responsible for intensity fluctuations [2,28]. It is important to note, however, τ is *not* the structural relaxation time unless $\beta = 1$, as when $\beta < 1$, many distinct decay processes contribute to g_1. For a stretched exponential decay, the average structural relaxation time is given by

$$\langle \tau \rangle = \frac{\tau}{\beta} \cdot \int_0^\infty x^{(1/\beta)-1} \cdot e^{-x}\, dx = \frac{\tau}{\beta} \cdot \Gamma\left(\frac{1}{\beta}\right), \tag{2.3.7}$$

where $\Gamma(1/\beta)$ is the *gamma function*, not to be confused with the decay rate, Γ (see appendix 7.2) [19,27,33].

The choice of functional form is entirely dependent on the system being studied and varies based on observations. Generally, the single-exponential exponent for diffusion is expressed as $-\Gamma t$, where $\Gamma = 1/\tau$ is the *decay rate* of g_1. For Brownian motion, $D =$ (characteristic length)^2/(time scale of diffusion) $\sim q^{-2}/\Gamma^{-1}$, therefore, $\Gamma = Dq^2$, where D is the *diffusion coefficient* [28]. In this case, the polymer chains remain correlated in a region of size ξ, the *correlation length*, and the Stokes-Einstein relation predicts

$$D = \frac{kT}{6\pi\eta_s\xi}, \tag{2.3.8}$$

for temperature T and solvent viscosity η_s. For uniform spheres in a viscous medium, $\xi = R$ is an estimate for the hydrodynamic radius of the spheres (effective size of a diffusing particle in solution), while for a polymer solution in the gel state, ξ gives an estimate of the *mesh size* ($\sim$ distance between polymer cross-links) [2,28,38,39]. For more complex dynamics, $\bar{\Gamma} = Dq^\gamma$, the exponent γ is not necessarily 2 (and not necessarily $\in \mathbb{Z}$) and can vary significantly depending on the system, while some relaxations may not be q-dependent at all [19]. For example, Einaga and Karube (1998) demonstrated a q-independent slow mode in a semi-dilute polymer gel. For these cases, where $\gamma \neq 2$, D is no longer the diffusion coefficient, instead, is a general *dynamical coefficient*.

The data analysis performed in this study of PAAA gel systems was focused on g_1. Importantly, the measurable intensity ACF, g_2, can be directly related to the electric field ACF g_1. For an ergodic system, averages taken over all points of a sample (or taken over multiple identical samples), $\langle I \rangle_E$, and averages taken over time for one section of the sample, $\langle I \rangle_T$, are identical. If the system is ergodic and the scattered electric field has a Gaussian power distribution, the *Siegert relation* is valid (see appendix 7.3) [2,33,40]:

$$g_2(t) = 1 + \tilde{\beta}|g_1(t)|^2 \quad \Rightarrow \quad g_1(t) = \left(\frac{g_2(t) - 1}{\tilde{\beta}}\right)^{1/2}, \tag{2.3.9}$$

where $\tilde{\beta}$ is the *coherence factor*, an empirical parameter close to 1 relating the size of the detector to the size of the observed region of the speckle pattern [2,16,41]. For monodisperse and polydisperse systems with minimal interaction between chains, as well as colloidal suspensions, equation 2.3.9 is a valid. In non-ergodic systems, where $\langle I \rangle_E$ and $\langle I \rangle_T$ differ, equation 2.3.9 yields unphysical results, commonly associated with gelation in polymer gels, as regions of the sample may remain bound when observed over time, leading to long lasting correlation. Measurements of a non-ergodic system generally do not capture the entire dynamics of the system, as only a small subset of the possible configurations of the sample are observed at one time [35]. Figure 2.3.4 demonstrates how one may observe the effects of the above discussion on the profile of the correlation functions [42]. At the smallest length scales ($\theta = 120°$), correlations between neighbouring regions of the sample diminish to zero. The probed region is small enough to observe non-correlated fluctuations in the intensity profile of the speckle pattern, indicating an ergodic system [32]. At larger length

scales (lower scattering angles), g_1 does not decay to zero, indicative of very slow relaxations or a non-ergodic system. Plateaus in the correlation functions at large lag times are suggestive of long-time correlation in the intensity profile (i.e. parts of the sample remain bound through physical cross-links – gelation), as such, averages taken over the whole system will **not** be identical to regional averages taken over time.

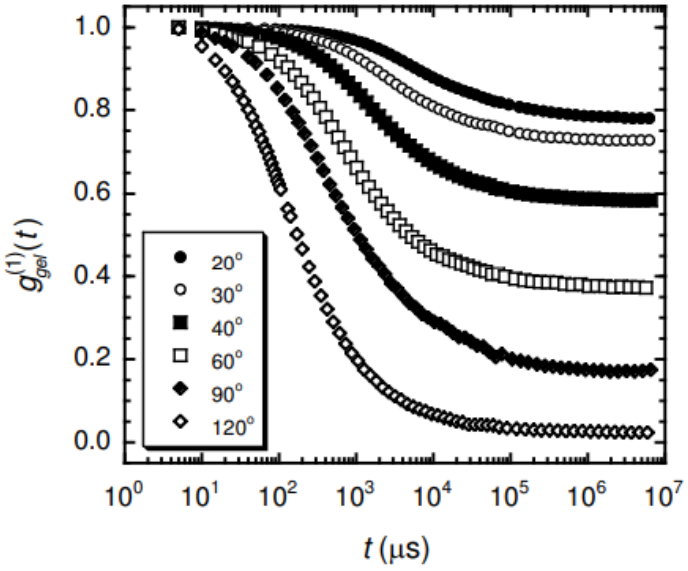

Figure 2.3.4. An indication of the switch between the ergodic and non-ergodic regimes in the electric field autocorrelation functions of a polymer gel. This switch occurs when observing the solution at differing length scales. The lowest curve represents observation at the smallest length scales, and vice versa for the highest curve [42].

A common method of estimating g_1 for non-ergodic systems is Pusey averaging [32,43], whereby the sample is slowly and continuously rotated while intensity averages are taken over time, measuring an ensemble average, $\langle I \rangle_E$, due to rotation. The usually stand-alone $g_2 - 1$ is combined with the measured $\langle I \rangle_E$, to approximately capture the dynamics of all configurations of the system, effectively reproducing what one would expect for an ergodic system, for a non-ergodic system [35]. For these cases,

$$g_1(t) = \frac{Y-1}{Y} + \frac{1}{Y}\sqrt{\tilde{g}_2(t) - \sigma}, \tag{2.3.10}$$

where $Y = \langle I \rangle_E / \langle I \rangle_T$, $\tilde{g}_2$ is the *normalised* intensity ACF, equal to $1 + (g_2 - 1)/\tilde{\beta}$, and σ is the short-time intercept of $\tilde{g}_2 - 1$ [18,32,44]. Thus, one would expect $Y \approx 1$ for an ergodic system - reducing equation 2.3.10 to equation 2.3.9 ($\sigma \to 1$ and $(Y - 1/Y) \to 0$), and $Y \neq 1$ for a non-ergodic system. Generally, one would expect $Y < 1$ for a non-ergodic system, and the consequences of $Y > 1$ are unreported in literature.

The relaxation regimes present in g_1 or $g_2 - 1$, in the sol phase, are commonly shown to be an initial fast mode and a more complex slow mode ('fast' implies short τ and vice versa), differing by several orders of magnitude in time [39]. The fast mode is almost unanimously agreed to be diffusive ($\gamma = 2$), while the slow mode is seen to vary significantly across literature. In the gel phase, the slow mode vanishes, with the ACF decaying to a finite plateau level [35]. A small intermediate regime is also reported in literature [7,45], however there is not much agreement in how this mode is analysed, and whether the q-dependence is consistent between gel systems. To better understand the important dynamics within gels for industrial applications, literature focuses on the shapes, approximate functional forms, and notable features of $g_2 - 1$ or g_1. Such features are indicative of the nature of the dynamics occurring in gels, which can be studied at various length scales through choice of q. $\bar{\Gamma}$ depends on q in a way which aids in the choice of appropriate polymer model. For example, the Rouse, Zimm and reptation models predict $\bar{\Gamma} \sim q^4$, $\bar{\Gamma} \sim q^3$ and $\bar{\Gamma} \sim q^{3.4}$ respectively (see

appendix 7.4). The fitting of analytical functions to the correlation functions provides information about the motions within the gel, as well as q dependencies, thus was the primary focus of this study.

3 Experimental methods

3.1 Initial data gathering and analysis

Autocorrelation data was provided by Dr. Johan Mattsson of the University of Leeds, recorded between 07/01/2004 and 03/11/2005. PAAA sample of concentrations 0.75wt%, 1.09wt%, 1.11wt%, 2.14wt% and 3.79wt% were used, where wt% denotes the proportion of dissolved mass of PAAA polymer compared to the total sample mass. The refractive index of water, n, and laser wavelength, λ_0, were measured to be 1.332 and 514.5nm respectively. The ALV5000 spectrometer was used to gather data across the five samples, through variation of the detector angle (*q-runs*) and temperature (*T-runs*), to investigate the effects of changing q at constant T and c and vice versa for investigating the effects of changing T. θ was typically varied between $20°$ and $140°$ at constant T for q-runs, and T varied between 298K and 350K at constant q (usually at $\theta = 30°$). Raw data from the output of the spectrometer is given in the form of lag time, t, in milliseconds and $g_2 - 1$ as a two-column array (see appendix 7.5 for example). Fluctuation measurements were taken over a period of around $2700s$ (45 minutes) to allow for a wide range of lag times to be used – between 10^{-5}ms and 10^{6}ms. This is necessary to capture the full range of dynamics within the gel, as mentioned previously, structural relaxation times can exist across many orders of magnitude. Python 3.7 was chosen for data plotting/calculations due to its ability to quickly compute using arrays (NumPy and Matplotlib packages), and easy visualisation of data. Raw $g_2 - 1$ was first investigated by eye, to assess the variation in shape, breadth, and plateau levels, to assess how one should analyse the data. $g_2 - 1$ data is then easily converted into g_1 data for ergodic and non-ergodic systems using equations 2.3.8 and 2.3.9, however it is considerably messier to revert the calculated g_1 back into g_2. Additionally, as mentioned previously, g_1 is a better representation of the dynamics occurring within the gel, directly related to the density fluctuations [2]. Thus, it was chosen to analyse g_1 in this study.

In addition to raw $g_2 - 1$ data, the ALV5000 spectrometer was ran for a shorter time ($\sim 30\text{s}$), while slowly rotating the sample – generating ensemble averages, $\langle I \rangle_E$ [32]. Intensity averages had to be further averaged across the spectrometer's two detectors – the count rates were almost always in the vicinity of one another, so this was unlikely to introduce many errors. Estimates for the parameter $Y = \langle I \rangle_E / \langle I \rangle_T$ were calculated for each individual dataset of all q-runs and T-runs, where $\langle I \rangle_E$ and $\langle I \rangle_T$ are the ensemble and temporal intensity averages respectively. This was done, in part, to calculate g_1 for non-ergodic runs as well as to observe the gelation transition as a change in Y. Y should remain close to 1 above the critical temperature, T_c, estimated to be approximately the sol-gel transition temperature. The sharp change in Y *should* correspond to an increase in the large t plateau level of $g_2 - 1$, representing the gelation transition and switch from the ergodic to non-ergodic regime. For sets of data with no corresponding Pusey runs, the profile of $g_2 - 1$ was observed to deduce whether it was appropriate to assume $Y = 1$; i.e. if the data appeared ergodic to the eye. For all runs where no Pusey data file existed, the system was observed to be close to ergodic thus, $Y = 1$ was assumed for such runs.

The first n points of $g_2 - 1$ were fit with a least-squares linear profile, where n was chosen from direct observation of the decay profile, ensuring the level of $g_2 - 1$ had not decayed. A plot of $g_2 - 1$ vs t for the first n points (generally $n \lesssim 30$, although could be larger due to noise) provided an estimate for $\tilde{\beta}$, the

coherence factor, as the short-time intercept. Since $\tilde{\beta}$ is a physical parameter relating the scattered interference pattern to the photodetector area, it was assumed a consequence of the equipment, *not* a feature of a particular sample/measurement. Thus, $\tilde{\beta}$ was estimated for all angles with the value for each angle being the average intercept of $g_2 - 1$ over all samples. These values could then be used in conjunction with estimates for Y in equation 2.3.9 for the ergodic regime ($Y = 1$) and equation 2.3.10 for the non-ergodic regime ($Y \neq 1$), for any set of data. $Y < 1$ was expected for non-ergodic sets of data, while $Y > 1$ was assumed unphysical, although this is unclear. The ergodic regime was chosen as $0.95 < Y < 1.05$, a suitable range, modifying such a range did not affect the calculations a great deal.

3.2 Main focus – fast and slow relaxations

The calculated g_1 data was manipulated to extract information about the structural relaxation, gelation temperature, diffusion coefficients etc. Initially, plateau levels were studied, extracted using linear fits of zero gradient on the final portion of the decay. The g_1 data was then plotted in several ways to predict, for example, the q dependence of the fast mode. If g_1 can be expressed as in equation 2.3.6b, then $\log(-\log(g_1))$ should vary linearly with $\log(t)$ with a gradient equal to β (i.e. uniform sphere, Brownian motion approximation). A large portion of the analysis involved fitting least squares linear regimes to the first relaxation mode of the data, as this was a consistent analytical tool which helped to give an estimate for β, before any fitting had been performed. Furthermore, if g_1 can be expressed as in equation 2.3.5, then $\log(g_1) \propto \langle \Delta r^2(t) \rangle$ and thus a log-log plot of $\langle \Delta r^2(t) \rangle$ and t reveals information about the trends in mean square displacement of diffusing particles, as a function of q or T. This is demonstrated in figure 3.2.1.

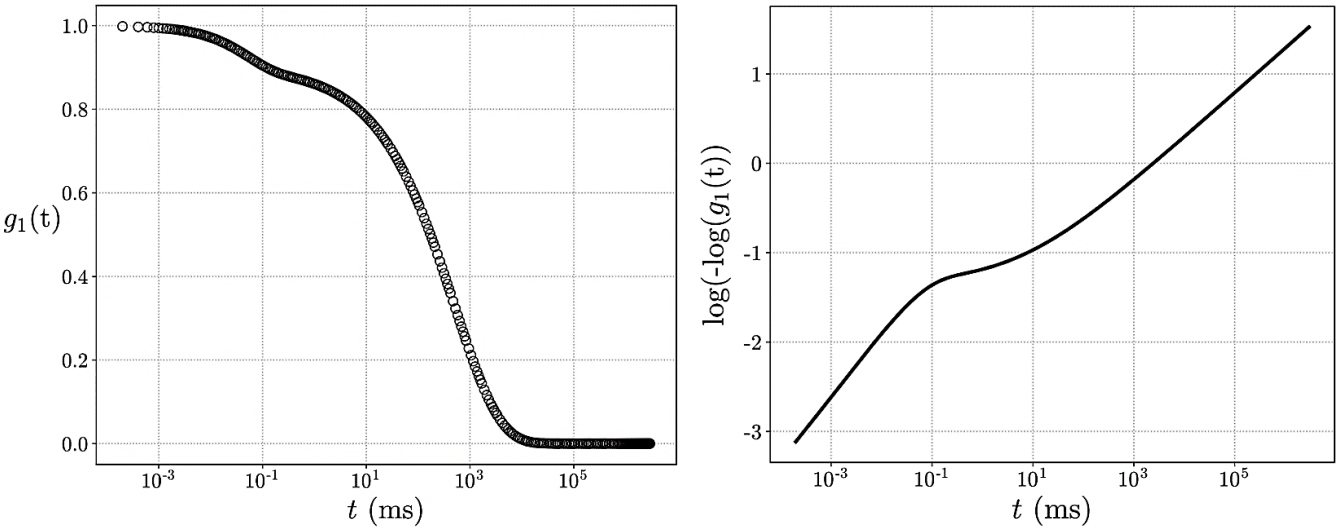

Figure 3.2.1. Left: simulated g_1 for PAAA in the sol state comprised of an addition of two stretched exponential decays with $\beta_1 = 0.8$, $\tau_1 = 0.05\text{ms}$ and $\beta_2 = 0.5$, $\tau_2 = 500\text{ms}$. The slow mode stretched amplitude is $\sim 9\times$ larger than the fast mode stretched amplitude. Right: linearised data demonstrating the gradual change of gradient as the slow mode is approached. The upwards trend is indicative of the increasing mean square displacement $\sim$ the paths taken by polymer chains increase in size as the relaxation time is increased, as expected.

In addition to this, if $\log(g_1)$ is scaled by a coefficient, a, and t is scaled by q^γ, then all curves $\log(-a \cdot \log(g_1))$ vs tq^γ for a q-run can be collapsed. This suggests the fluctuations and dynamics producing the intensity ACF are unchanged/comparable across the length scales probed in the system. This was generally only performed with the fast mode for $\gamma = 2$, as it was believed the slow and intermediate modes would be significantly more difficult to rescale this way.

The scaling constants, a, were successively and manually chosen, normalised to $a = 1$ for the lowest q curve. An automatic method of choosing the scaling constants was not known, thus, a model fit was implemented which could then be utilised for other q-runs, a power-law, $a \sim q^{\alpha}$, being predicted. This process was repeated for the remaining q-runs, although could not be performed for T-runs, as the curves were found to vary with T in an unpredictable way (although general trends such as the change in curve shape from below T_c to above T_c could be predicted). The aim of rescaling was to predict the underlying dynamics of the fast relaxation, thus the q-dependencies for $\langle\tau\rangle, \bar{\Gamma}$.

Both the fast and slow relaxations were chosen to be fit with stretched exponentials of the form:

$$g_1(t) = Ae^{-\left(\frac{t}{\tau}\right)^{\beta}} + B, \tag{3.2.1}$$

for amplitude A and baseline B, generally done separately due to the unknown form of the intermediate relaxation. In some cases, the intermediate mode appeared suppressed, thus a sum of stretched exponentials was used instead:

$$g_1(t) = Ae^{-\left(\frac{t}{\tau_1}\right)^{\beta_1}} + (1 - A)e^{-\left(\frac{t}{\tau_2}\right)^{\beta_2}}, \tag{3.2.2}$$

as $g_1(t)$ was assumed to begin at an amplitude of 1, so the amplitudes of each mode must sum to 1. Fitting was performed in OriginLab, chosen due to its speed in changing the size of the fitting region, as well as being able to visually assess the quality of the fits in real-time. The parameters in equations 3.2.1 and 3.2.2 were generally left free until suitable choices could be made, for instance for A, several curves were fit before a reasonable idea for the amplitude change from one regime to the next was developed. A could then be fixed using a reasonable estimate for this amplitude difference. In addition to using equation 3.2.1 with free parameters A and B, it was also implemented under the strict condition $A + B = 1$, as the decay should theoretically begin from 1. The choice of either case was entirely dependent on the quality of the least squares fit, as in some cases one would work significantly better than the other.

3.3 Fitting to the intermediate regime

A suitable analytical function for the intermediate relaxation was more difficult to find. It has been reported in literature [7] this regime may be power law dependent, as such, this was attempted for a range of datasets. Power-law relaxations are suggested as a feature of gelation, indicative of the non-ergodic nature of the system [7,45]. The end of the fast mode and the beginning of the slow mode were determined by eye to split the data at each end and isolate the intermediate region. A log-log plot of g_1 vs t should reveal a linear relationship in the intermediate relaxation if power-law behaviour is present. Thus, log-log plots were generated for the spliced data for a range of temperatures of the 1.11% sample. The gradient of a least squares linear fit to this region is the α-exponent in equation 2.3.6a, with the intercept being a proportionality constant. Once suitable fits were established, the entire decay of g_1 could be expressed according to equation 3.3.1:

$$g_1(t) = Ae^{-\left(\frac{t}{\tau_1}\right)^{\beta_1}} + Bt^{-\alpha} + (1 - A - B)e^{-\left(\frac{t}{\tau_2}\right)^{\beta_2}}, \tag{3.3.1}$$

leaving 7 independent free parameters for the fit. In cases where a power-law seemed like an unsuitable fit, equation 3.3.2 was used instead:

$$g_1(t) = Ae^{-\left(\frac{t}{\tau_1}\right)^{\beta_1}} + Be^{-\left(\frac{t}{\tau_2}\right)^{\beta_2}} + (1 - A - B)e^{-\left(\frac{t}{\tau_3}\right)^{\beta_3}}, \quad (3.3.2)$$

leaving 8 independent free parameters. Problems arise from the large number of free parameters, as multiple separate combinations of these parameters could equally be used to fit to the data. Thus, a way of relating the parameters to one another was attempted, although largely unsuccessfully.

Stretched exponentials and power-laws may not be the only viable fitting functions for autocorrelation data. To reproduce the behaviour shown in the right-hand plot of figure 3.2.1, one requires some form of double exponential function. Thus, any function which can reproduce this linear behaviour for separate regimes can be used to express the combination of two of the regimes. For example, if τ_1, β_1, A and τ_2, β_2, B in equation 3.3.2 can be related to each other, the number of free parameters is reduced to 5 and the number of degenerate fits is thus reduced. The choice of functions distinct from those in equation 3.3.2 is scarcely reported in literature, thus a model had to be developed. An attempt was made with the function

$$g_1(t) = A \cdot \exp\left[b \cdot \left\{1 - \exp(-(t/\tau)^{\beta}\right\}\right], \quad (3.3.3)$$

used to fit only the fast and intermediate regimes. This found some success in fitting, although it was unclear whether it was a suitable function to describe the underlying physics. Log-log plots of equation 3.3.3 do provide the same form as shown in figure 3.2.1, however this function only appeared to fit well to datasets with suppressed intermediate relaxations, defeating the purpose of this exercise. Nonetheless, this method was used in conjunction with a stretched exponential for the final relaxation:

$$g_1(t) = A \cdot \exp\left[b \cdot \left\{1 - \exp\left(-(t/\tau_1)^{\beta_1}\right)\right\}\right] + (1 - A)e^{-\left(t/\tau_2\right)^{\beta_2}}, \quad (3.3.4)$$

with the aim of fitting the whole decay profile. Some simulated data for the appearance of equation 3.3.4 is shown in figure 3.3.1.

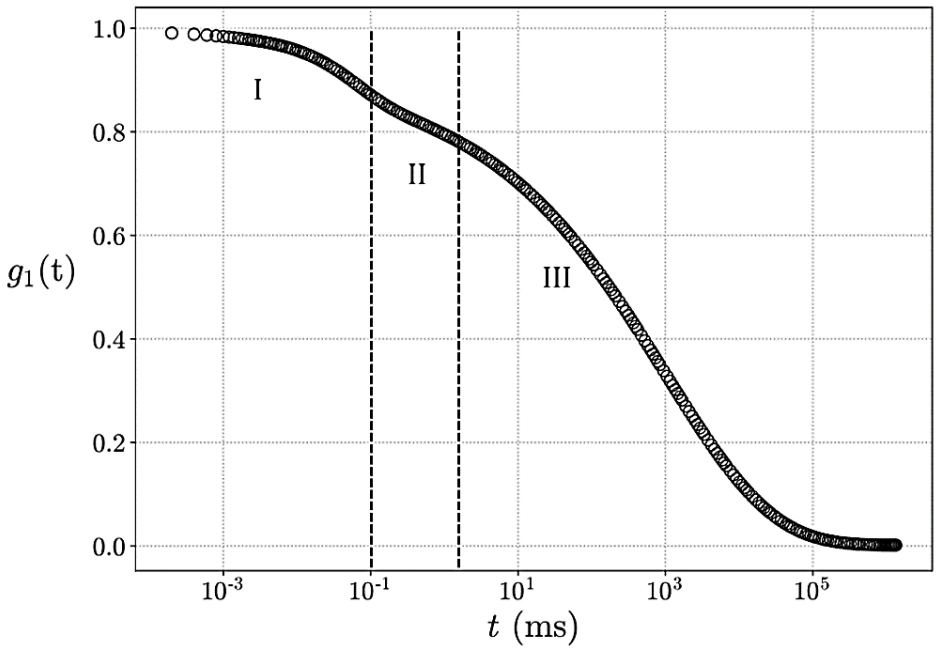

Figure 3.3.1. Simulated data of the form shown in equation 3.3.4. The fast mode (I) and intermediate mode (II) are fit together according to the first term, with parameters $A = 0.1, b = -4, \tau_1 = 0.2\text{ms}$ and $\beta_1 = 0.8$. The slow mode (III) is a stretched exponential with parameters $\tau_2 = 1s$ and $\beta_2 = 0.3$. This curve simulates a potential full decay fit with 6 free parameters, a marginal improvement over the other methods.

Importantly, equations 3.3.1/3.3.2/3.3.4 can be applied to the whole decay, or more usefully, the data can be spliced to fit each term of the function to regions $(\text{I}), (\text{II}), (\text{III})$ separately. For example, the power-law in

equation 3.3.1 may not be an accurate description of the physics of the fast mode nor the slow mode and should not be significant in these regimes. Generally, this found more success than fitting the entire function to all regions.

4 Results and Discussion

4.1 Initial observations

Calculations of $Y = \langle I \rangle_E / \langle I \rangle_T$ for all sets of data with separate Pusey measurements yielded interesting and unexpected results, deviating significantly from 1 for most of the data. Figure 4.1.1 demonstrates the change in Y as the probed length scale is decreased (q increased), the trends approximately show the system appears more ergodic for larger observed regions. This makes intuitive sense, as the greater the size of the probed region, the greater the chance of observing uncorrelated behaviour in the gel, such that it appears more homogeneous. Figure 4.1.2 shows the trend in Y as the concentration is varied for T-runs.

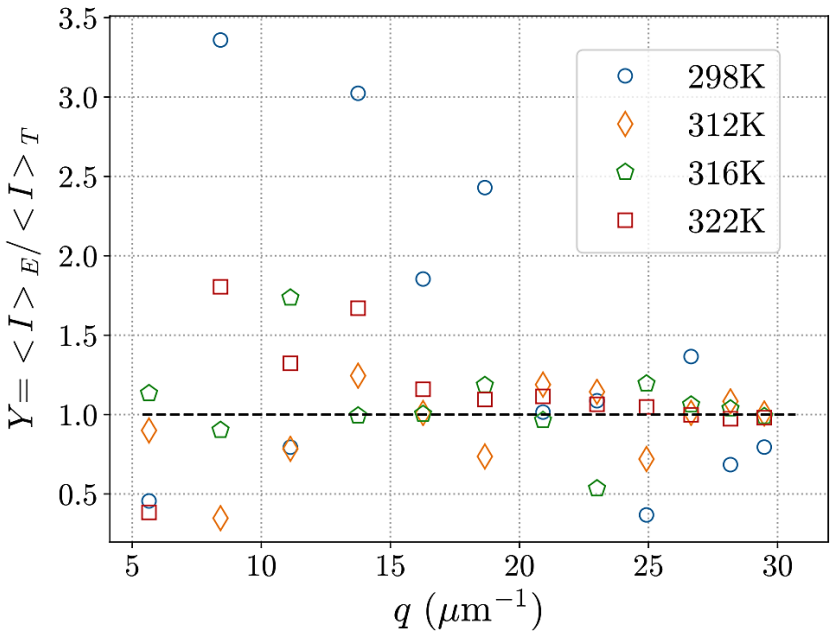

Figure 4.1.1. Calculated Y values for q-runs across four temperatures. The dotted line represents the expected ratio from theory for an ergodic system.

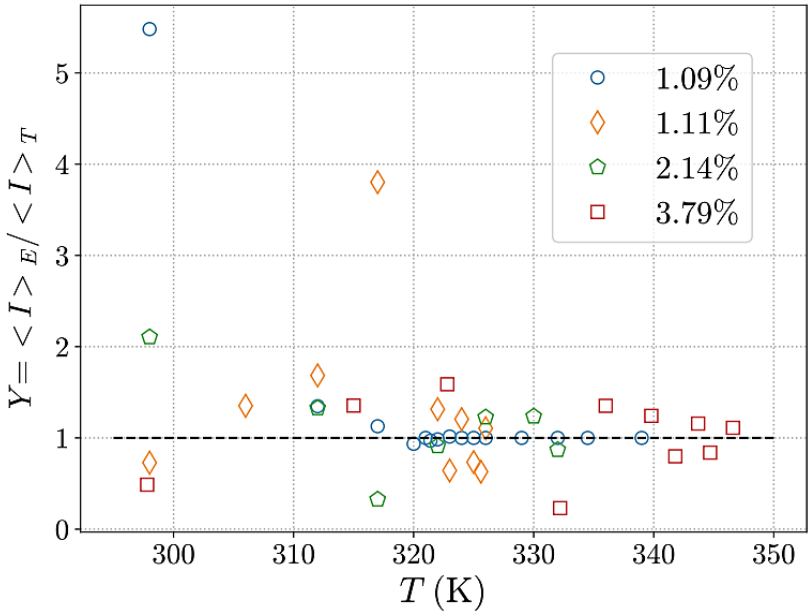

Figure 4.1.2. Calculated Y values for T-runs across four concentrations. The dotted line represents the expected ratio from theory for an ergodic system.

Aside from the results which do not conform to this trend, Y appears to cluster around 1 for all concentrations, indicating Y may not be concentration dependent. For both sets of data, Y is frequently found to be > 1; it is unclear whether this is caused by a real physical mechanism or a result of errors, possibly due to the presence of scattering from dust particles in the sample. For example, consider the peak in Y at $T = 317\text{K}$ for the 1.11% sample in figure 4.1.2, which appears to be a result of scattering from a foreign source such as a dust particle, not a physical consequence of the dynamics in the gel. Figure 4.1.3 demonstrates this.

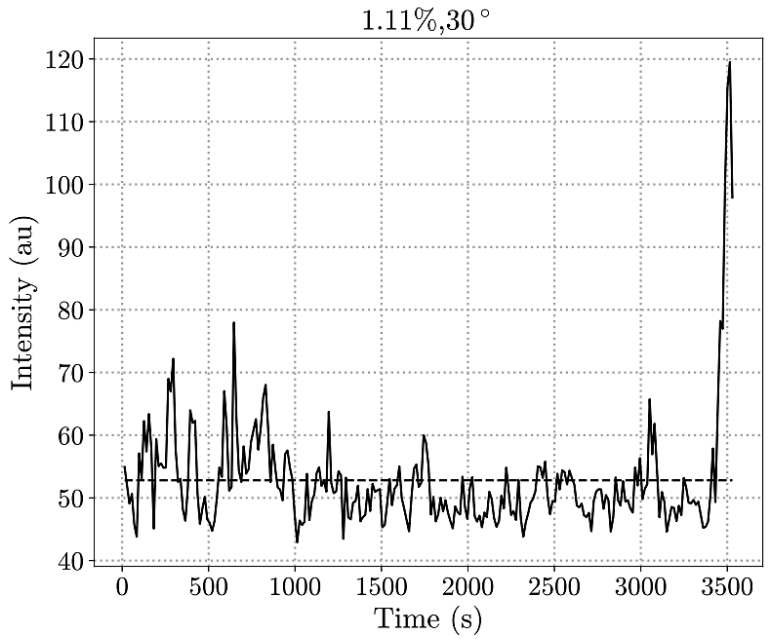

Figure 4.1.3. Intensity trace for the 1.11% sample at $\theta = 30°$ and $T = 317\text{K}$. The dotted line is the time-averaged intensity, $\langle I \rangle_T$.

The large spike in the count rate at $\sim 3500s$ is suggestive of scattering from such a foreign source. In this case, it is not appropriate to take an average over all times, as it is skewed greatly by this peak.

A similar analysis was performed to calculate the coherence factors, $\tilde{\beta}$, relating the size of the observed region of the speckle pattern to the size of the detector. In theory, these sizes should be the similar, if not the same, thus $\tilde{\beta} = 1$. In fact, $\tilde{\beta}$ decreases approximately linearly with increasing q, possibly being due to the spreading of the speckle pattern for wider angles; shown in figure 4.1.4.

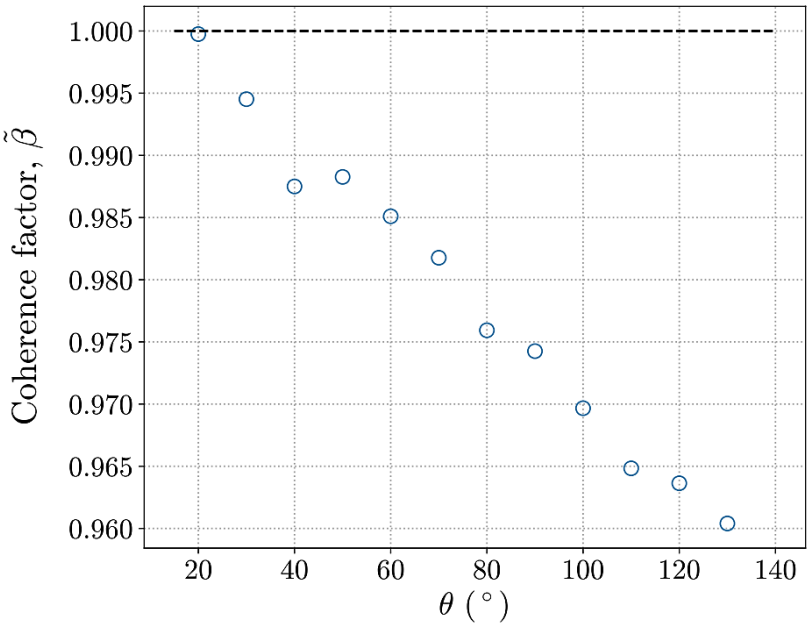

Figure 4.1.4. Coherence factors calculated from averages across all samples for each detector angle, θ. The dotted line is $\tilde{\beta} = 1$.

This behaviour is very systematic, suggesting it is a consequence of the experimental setup, rather than resulting from any measurement or calculation error.

All g_1 for a specific detector angle were calculated using equations 2.3.9 and 2.3.10 utilising the coherence factors from figure 4.1.4. Observations of the shape and features of g_1 for all concentrations were consistent with the theory, 1.11% q-runs are shown in figure 4.1.5.

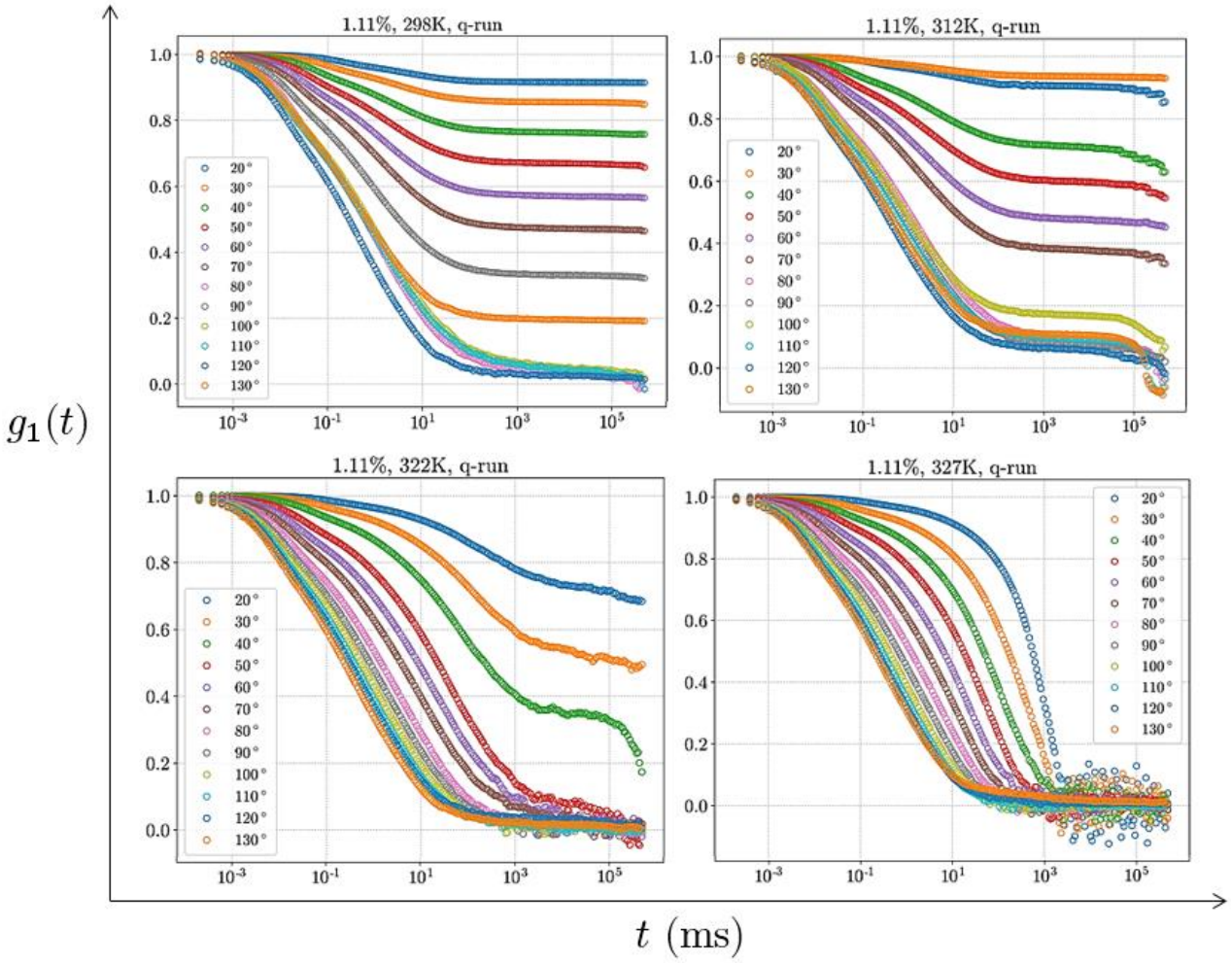

Figure 4.1.5. Electric field ACF q-runs for the 1.11% sample at all temperatures ($298\text{K}, 312\text{K}, 322\text{K}, 327\text{K}$). The broadest decays represent the lowest scattering angle, 20°, and the sharpest decays represent the highest scattering angle, 130°, corresponding to the largest and smallest probed length scales respectively.

Notice the change in shape of the curves as q, and hence the probed length scale, is changed. Each curve consists of an initial decay, followed by an intermediate region and then a broader decay at large t. The intermediate decay is significantly suppressed in this set of data, possibly due to the comparatively low concentration by weight of the sample. Also note the increase in noise at long lag times for the higher temperatures, attributed to an amplification in thermal fluctuations due to the squaring of noise in $g_2 - 1$. The gelation transition can clearly be observed in figure 4.1.5. At 298K (room temp), PAAA is shown to exist in the gel state, corresponding to a high elastic modulus and plateau level, agreeing with the observations of Marstokk et. al. (1998) and Ostrovskii et. al. (1999). At larger t, the intensity fluctuations remain correlated, suggestive of persistent cross-links between polymer chains. As q is increased, the plateau level decreases (in general), which is consistent with what is expected [19] – increasing q decreases the probed length scale, increasing the chances of observing uncorrelated, thermal motions of individual chains or monomers [18]. This behaviour is consistent for all temperatures aside from 327K, and for the higher temperatures, the intensity fluctuations for larger q become completely uncorrelated ($g_1 \to 0$). The characteristic length scale in

which gelation is observed can be estimated from the point at which g_1 completely decays to zero, as opposed to decaying to a finite plateau. For example, in the $298\mathrm{K}$ data, the data becomes uncorrelated at $\theta_c \approx 100°$, suggesting the probed scale, l, for observing the gel phase at this temperature is $l_c \gtrsim 0.25\mu\mathrm{m}$ ($l \approx 2\pi/q_c$). As the temperature is increased, the data becomes uncorrelated at lower θ, suggesting l increases with temperature – larger length scales must be observed to see correlations. l eventually diverges ($\theta_c \to 0$) when the sample is entirely in the sol state, as shown in the $327\mathrm{K}$ curves (consistent decay to zero for all θ).

Figure 4.1.6 is akin to the plots in figure 4.1.5, but for constant q and changing T. $298\mathrm{K}$ data is omitted here as it was anomalous, with intensity trace similar in appearance to figure 4.1.3.

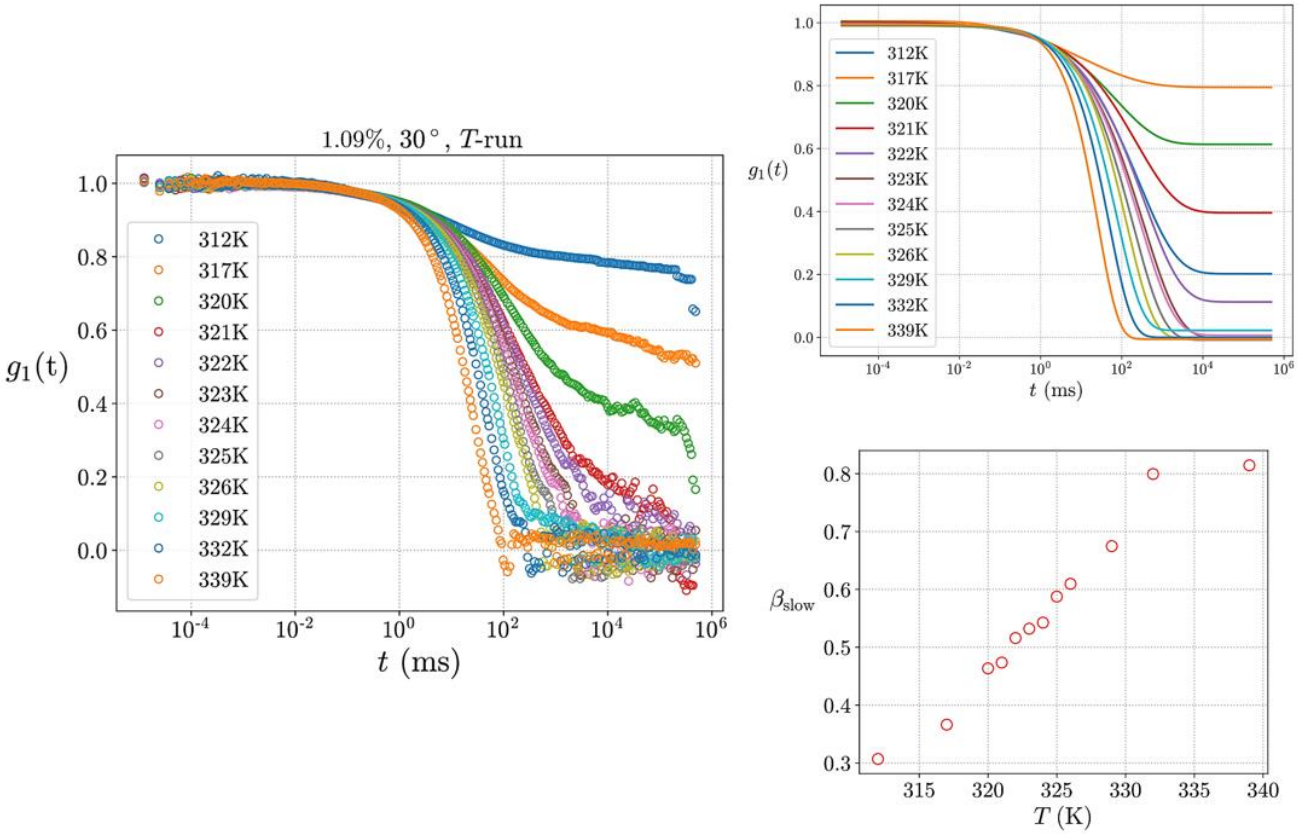

Figure 4.1.6. Electric field ACF T-run for the 1.09% sample at $\theta = 30°$. The broadest decay represents the lowest temperature, $312\mathrm{K}$, and the sharpest decay represents the highest temperature, $339\mathrm{K}$. The upper-right panel shows double stretched exponential fits to the data, with the lower-right panel a plot of the slow relaxation stretching parameters across the temperature range. Note the stretched exponential fits decay to a finite plateau by design, while the raw data appears to 'tail off' – this is deemed unphysical as any minute fluctuation during the large gap in time can cause such behaviour.

The gelation transition can clearly be observed here, as the long-time plateau decreases as a function of temperature, until it is approximately zero. At $312\mathrm{K}$ the sample is mostly frozen at large t, indicating correlations between neighbouring polymer chains are still significant. Similarly to the collapsing of g_1 in the q-run above, in figure 4.1.6, curves for all T are collapsed up to a lag time $t \approx 1\mathrm{ms}$. This collapsing occurs despite no rescaling of either axis being performed. Thus, the fast and intermediate modes may decay in consistent ways, unaffected by the increase in temperature. The slow mode is significantly altered through heating, however, and the motions in the gel become uncorrelated at shorter times at higher T. This is expected, as PAAA forms a gel at ~ room temperature, thus, should be significantly further into the sol phase at higher T.

The long-time plateau observed in all curves is a consequence of the gel phase, varying non-linearly with q, however, more data is needed to make solid conclusions about the relationship. Plateau levels for the 1.11% sample across the full q range are shown in figure 4.1.7.

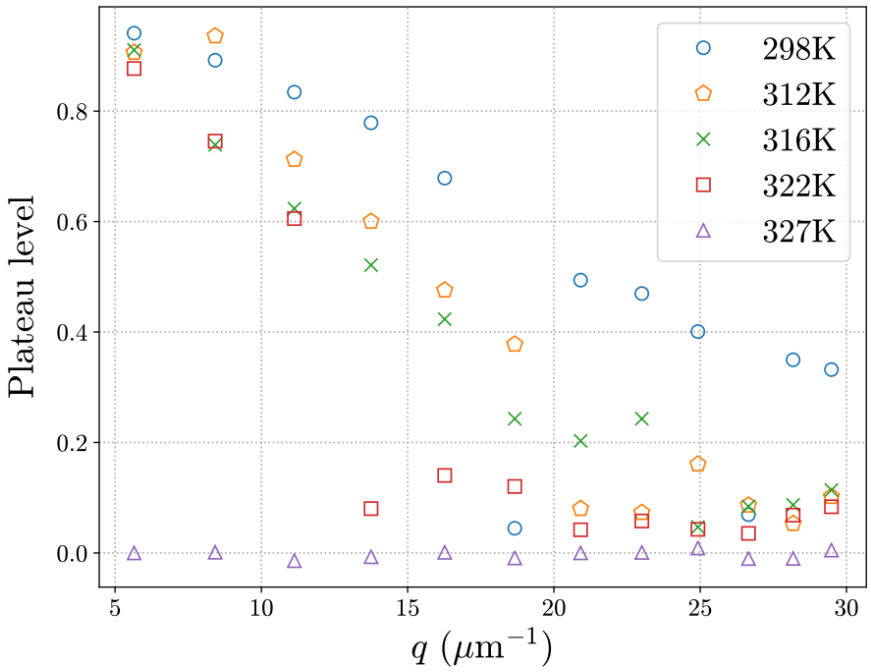

Figure 4.1.7. Variation in the finite plateau with q for the 1.11% sample for each temperature. The plateau decreases with q in a non-linear fashion for all temperatures except the highest (triangles), remaining close to zero for all q.

A comparison between the plateau levels of different concentrations was performed, although most of the data in this study was taken for $T > T_c$, i.e. most of the plateau levels were zero. The plateau level for lower concentrations was in general lower and decreased with T_c, suggesting T_c increases as a function of c. This was intuitively predicted, as a higher concentration polymer will form more cross-links, the mesh size should decrease, thus predicting larger long-time correlation. Figure 4.1.8 shows a change in the plateau level across three temperatures for three of the samples.

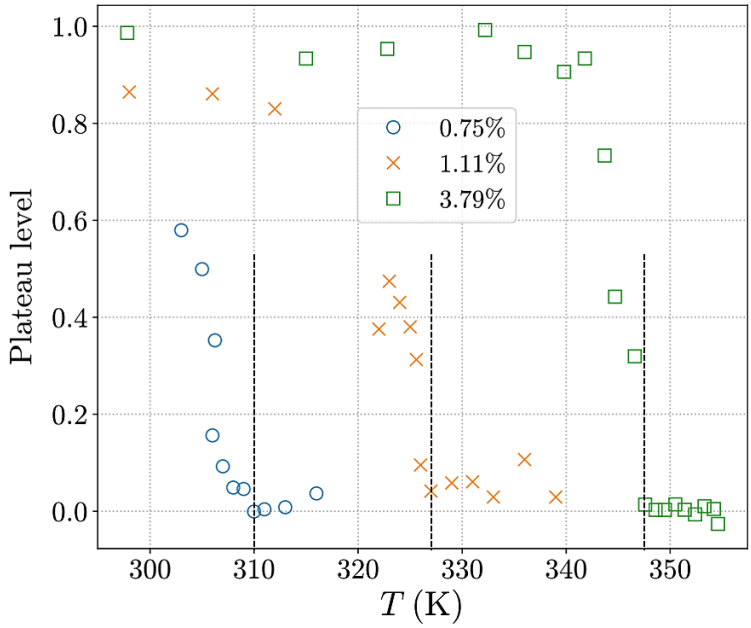

Figure 4.1.8. Variation in the finite plateau with T for the lowest, middle, and highest concentrations. The scattering angle for all data points was 30°. The dotted line represents an estimate for the sol-gel transition temperature.

The lowest concentration, 0.75%, exhibited significantly lower correlation even at room temperature,

signifying that this concentration is not sufficient for sample-wide gelation at room temperature and must be cooled further. The plateau levels for each concentration decrease to ~ 0 at a temperature defined as T_c. The highest concentration is almost completely frozen at all temperatures below T_c, indicating a strong gel phase is present. For the other concentrations, the highest plateau is significantly lowered, as expected. The data suggests $T_{c,0.75} \sim 310\text{K}$, and $T_{c,1.11} \sim 327\text{K}$ and $T_{c,3.79} \sim 347\text{K}$.

A log-log plot of $-\log(g_1)$ vs t reveals information about the mean squared displacement, $\langle \Delta r^2(t) \rangle$, of motions within the gel. According to equations 2.3.5 and 2.3.6a, $\log(\langle \Delta r^2(t) \rangle) \propto \log(t)$, assuming the dynamics are simple diffusion via Brownian motion (i.e. scattering from uniform spheres). Generally, the motions within gels are **not** simple diffusion, although this comparison is still useful to see the trend when changing the concentration. Figure 4.1.9 demonstrates the change in the average path length taken in the intermediate relaxation over for timescales between $\sim 0.5\text{ms}$ and $\sim 1000\text{ms}$.

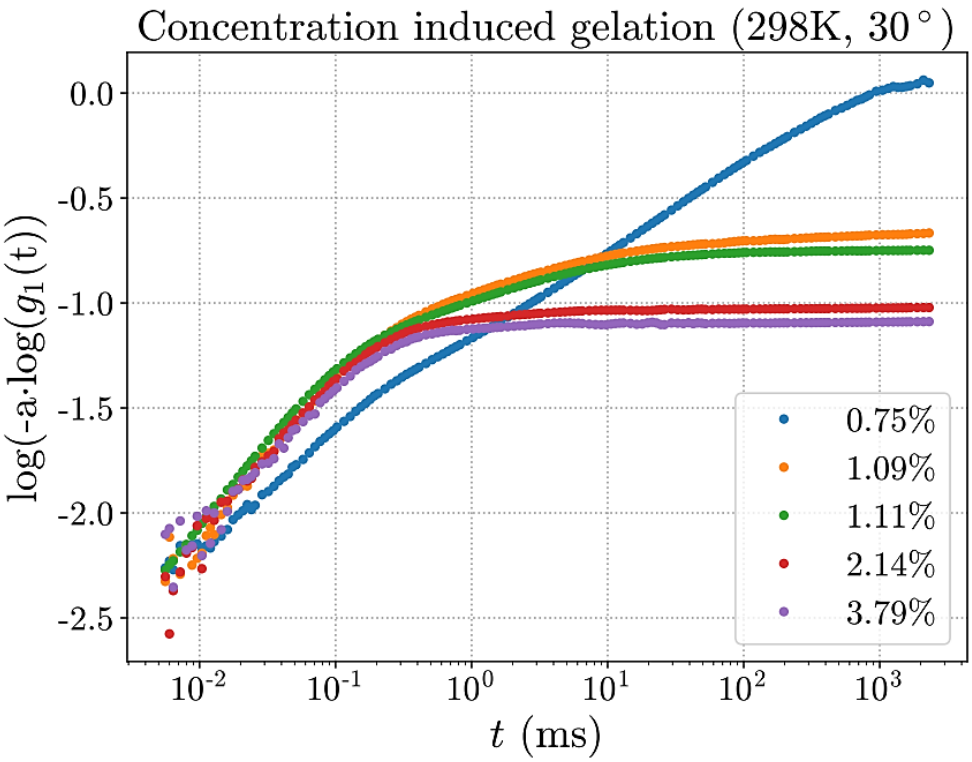

Figure 4.1.9. Mean squared displacements of the fast and intermediate regimes for all concentrations at room temperature (298K) and $\theta = 30°$. Each curve is scaled by an arbitrary constant, a, normalised as $a = 1$ for $c = 1.09\%$.

Each curve is scaled by a factor, a, to compare their forms directly. As a result, the plateau levels should not be considered equal to $\langle \Delta r^2(t) \rangle$, rather, are suggestive of the *trend* in $\langle \Delta r^2(t) \rangle$. As explained earlier, 0.75% by weight is not a sufficient concentration for inducing sample-wide gelation, hence the lack of finite plateau in $\langle \Delta r^2(t) \rangle$. The remaining concentrations follow expected trends: the polymer chains become increasingly frozen at shorter lag times as the concentration is increased, inducing the plateau at earlier times. Plus, increasing the concentration of polymer in solution decreases the total path length that chains can move, decreasing $\langle \Delta r^2(t) \rangle$. Notice the comparison between the simulated sol-state data (figure 3.2.1) compared to figure 4.1.9; the small plateau observed in figure 3.2.1 is stretched into a long-time plateau in figure 4.1.9 during the gel phase, indicative of a broader intermediate relaxation. This is indicative of a switch between an ergodic system ($c = 0.75\%$) to a non-ergodic system ($c > 0.75\%$). The data in figure 4.1.9 eventually increases again after around 1000ms as the slow relaxation is approached, suggesting $\langle \Delta r^2(t) \rangle$ increases again as measurements are taken further apart (large t).

4.2 Results from analytical fits to the fast and slow regimes

Rescaling of the fast mode predicted a strong q^{-2} dependence on the average relaxation rate. Figure 4.2.1 shows the collapsing of all curves in the highest temperature q-run of the 1.11% sample.

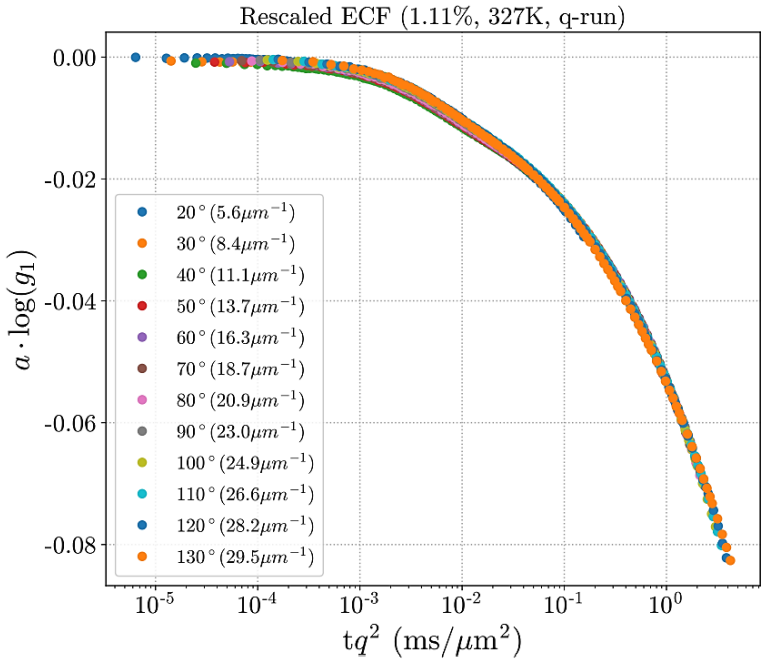

Figure 4.2.1. Collapsed log-log plot of rescaled g_1 vs the rescaled time axis, tq^2. The first $n = 100$ datapoints are shown here.

As mentioned in section 3.2, the scaling constants, a, were chosen manually and sequentially. Notable in figure 4.2.1 is the collapsing of the fast mode, the intermediate mode, and even a large portion of the slow mode, suggesting a good model for the description of the sum of these decays is simple diffusion by Brownian motion. The same choice of scaling constants for the entire decay shows disassociation for lag times greater than $t = 0.16\text{ms}$ ($tq^2 = 5\text{ms}/\mu\text{m}^2$), significantly into the slow relaxation regime. A power-law relationship between a and q was proposed, as plots of $\log(a)$ vs $\log(q)$ were generally linear, to develop a model for collapsing other datasets. However, the errors present in the power-law fit were too large to prove useful, thus, a was chosen manually throughout. The collapsed curves utilising this approximation are shown in figure 4.2.2.

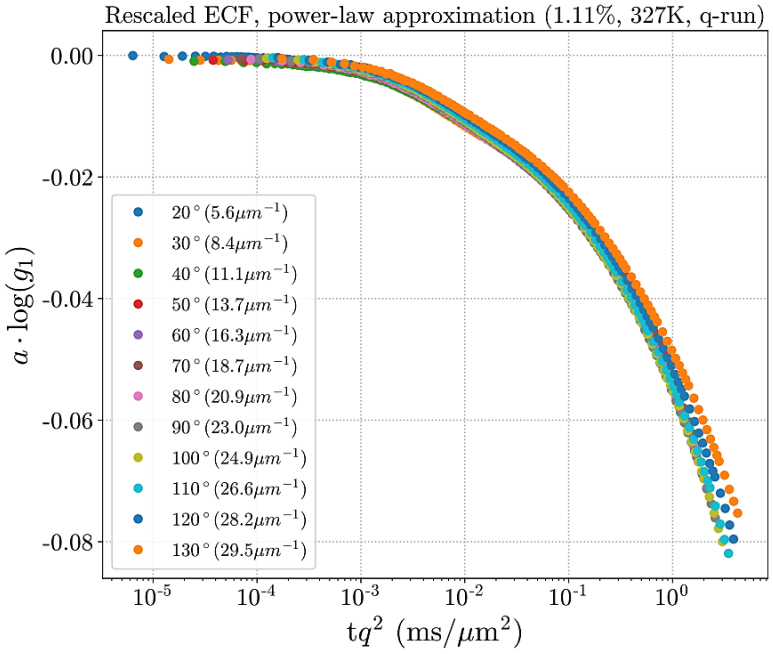

Figure 4.2.2. Collapsed log-log plot of rescaled g_1 vs the rescaled time axis, tq^2, using a power-law approximation, $a \propto q^{-\gamma}$. The first $n = 100$ datapoints are shown here. Notice the decorrelation at longer lag times – a result of errors in the power-law approximation.

The diffusive model was shown to fit well for all datasets of the 1.11% sample as similar collapsing of the curves was observed. Thus, to correlate the results, the collapsed datasets at different temperatures were assumed to be described by the same underlying physics. In this case, the power-law relationship between a and q should not vary significantly as the temperature is changed. This was confirmed, as the power-law fits were very consistent for each temperature. The relationship between a and q for this sample was found to be $a = Aq^{-\gamma}$ where A must have inverse units of $q^{-\gamma}$ as a is dimensionless, defined as u for simplicity. The averages are $A = (12.2 \pm 0.5)u$ and $\gamma = 1.41 \pm 0.1$. There was not enough data for the other concentrations, otherwise, this analysis would be repeated to see the effect of c on A and γ. The small error in γ is indicative of the small variation in slope of each of the log-log power-law curves in figures 4.2.3.

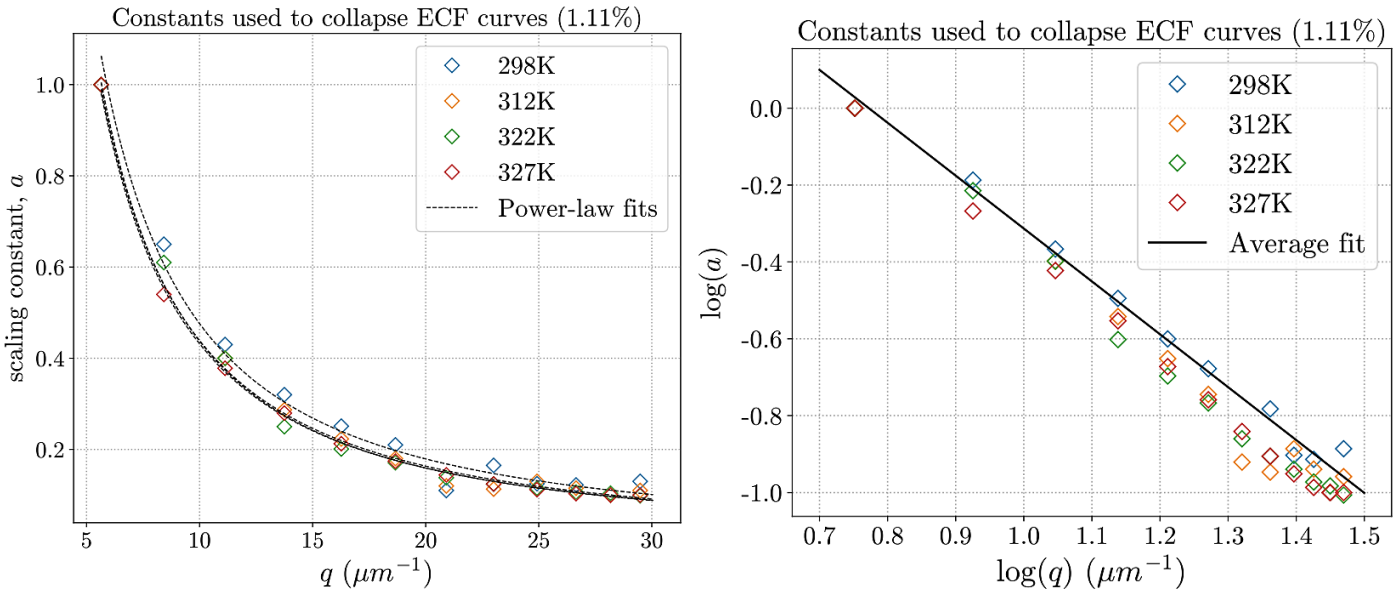

Figure 4.2.3. Manual scaling constants as a function of the scattering vector. All temperatures for the first 1.11% sample are shown here, with approximate power-law fits. The right panel is a logarithmic plot of a vs q, linearising the data from the left panel.

Most of the fitting performed in this study utilised equation 3.2.1 for the fast and slow modes. Both regimes were, in general, fit separately due to the intermediate mode which lies between, whereas, in some systems, the intermediate mode is unnoticeable and hence a fitting function such as equation 3.2.2 can be used for the entire decay [29,42,43]. Fits to the fast and slow regimes generated four parameters: amplitude, A, stretching parameter β, characteristic timescale τ and baseline B. β and τ are studied here, although A may be compared between each regime, to assess the relative size of each decay. The baseline, B, is precisely the plateau level for the slow mode, and has been discussed previously. The objective of studying τ was to assess the relationship between $\langle\tau\rangle$ and q. Diffusive dynamics was expected for the fast mode, $\langle\tau\rangle \propto q^{-2}$, and typically this is what was observed, whereas other motions were expected for the slow mode. However, Marstokk et. al. (1998) have reported a non-diffusive, q^{-3} dependent fast mode for PAAA dissolved in water, and a diffusive, q^{-2} dependent fast mode for PAAA dissolved in sodium thiocyanate from DLS studies. $\tau \sim q^{-3}$ is suggestive of Zimm behaviour, where hydrodynamic interactions between polymer chains and the solution are significant [10]. Figure 4.2.4 is a plot of the fast mode average relaxation times, $\langle\tau\rangle_f$, as a function of the concentration of PAAA in solution, at room temperature, 298K, and a higher temperature, 312K.

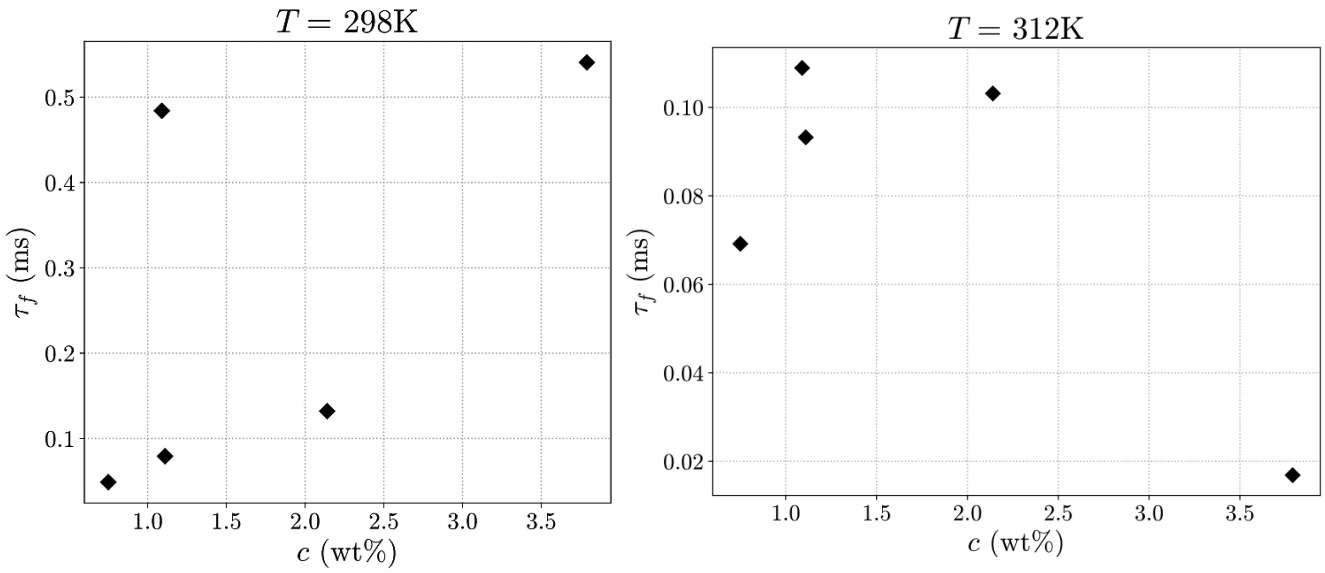

Figure 4.2.4. Fast relaxation characteristic decay times dependence on the polymer concentration by weight for two temperatures. The concentrations in order of increasing size are 0.75%, 1.09%, 1.11%, 2.14%, 3.79%. Average relaxation times are calculated using equation 2.3.7.

For $T = 298\mathrm{K}$, the relaxation appears to critically slow down, aside from the anomalous point from the 1.09% sample. For $T = 312\mathrm{K}$ however, the critical slowing down occurs only across the first three concentrations, suggesting that the temperature is low enough for these three samples to enter the gel phase. For concentrations 2.14% and 3.79%, there were large differences in the quality of the stretched fitting to the fast mode, and thus a large range of relaxation times. In general, however, the behaviour shown in figure 4.2.4 is what was seen for these two concentrations and does not appear to follow the trend from the $298\mathrm{K}$ data, nor the data presented by Marstokk et. al. (1998) in their study of PAAA in water, who showed a consistent upwards trend in the relaxation time as concentration is increased. The rescaling analysis predicts $\tau \sim q^{-2}$. Stretched exponential fits to the fast modes of each dataset in each q-run revealed a similar result, although there was significant variation in the exponent, generally between 1.7 and 2.5. On average, however, the fast mode appears diffusive as predicted. Decay rates for the first 1.11% sample are shown in figure 4.2.5.

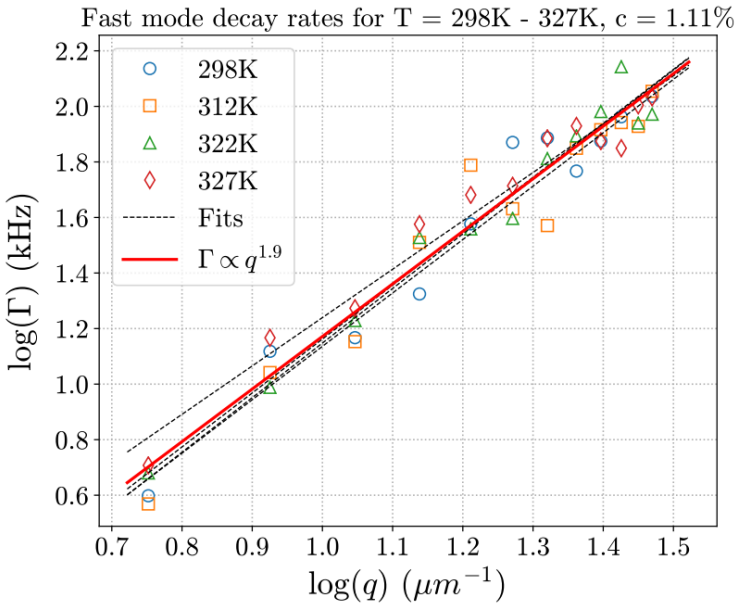

Figure 4.2.5. Fast mode decay rates from equation 2.3.7 for all data from the first 1.1% sample. The dotted lines represent the linear fit in the log-log plot to each temperature, while the red line represents the average linear fit.

The spread of data in figure 4.2.5 is significant, averaging to a linear fit for most data points. This suggests that a power-law is not perfectly representative of the relationship between $\bar{\Gamma}$ and q *for these specific parameters found*, rather, is a good approximation. Nonetheless, the average of all gradients is 1.9, suggesting cooperative diffusion is a good fit for the fast relaxation in this sample. The q dependencies of the slow mode decay rate for this sample were unpredictable, often deviating from linear relationships in a log-log plot. The most successful fits are shown in figure 4.2.6.

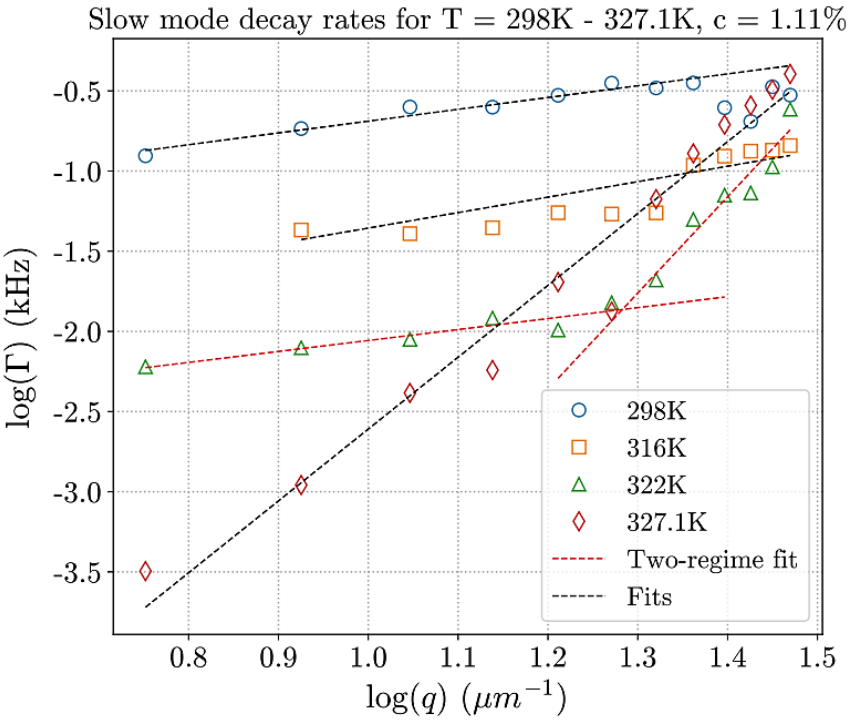

Figure 4.2.6. Slow mode decay rates calculated from equation 2.3.7 for all data from the second 1.11% sample. The dotted lines represent the linear fit in the log-log plot to each temperature, while the red dotted line represents a two-regime fit.

For the slow mode, the decay rates are noticeably more varied across the temperature range compared to for the fast mode. The gradients (γ-exponent) vary between approximately 0.7 and 6, suggesting a wide range of possible dynamics for the motions which produce the slow relaxation in g_1. Also, in some data sets a 'two-regime' fit was used – indicating there may be some switch in dynamics at a critical length scale.

From the fits to of the q dependence for the fast mode, the diffusion coefficient can be evaluated: $D \approx 10^{\text{intercept}}$. The cooperative diffusion coefficient is between $D_\text{f} = 2 \times 10^{-10}\ \text{m}^2/\text{s}$ and $D_\text{f} = 4 \times 10^{-10}\ \text{m}^2/\text{s}$, which appears to be around the range one would expect for this system (Marstokk et. al. (1998) report a diffusion coefficient of $1 \times 10^{-11}\ \text{m}^2/\text{s}$). The uncertainty is measured from the spread of the intercepts for all linear fits, although it is likely to be larger than stated. Uncertainties from the fits themselves and the calculated $\langle\tau\rangle$ must be accounted for, possibly increasing the quoted uncertainty significantly. For the slow mode, the dynamics are significantly more varied and thus calculation of D_s is more complicated. It may not be useful to calculate D in these cases, as it does not represent the coefficient of Brownian motion. If D_f is assumed constant for the 1.11% sample across the temperature range shown in figure 4.2.6, then the mesh size of the gel, ξ, varies with the viscosity of the solvent (water). Figure 4.2.7 is a demonstration of the decrease in ξ with decreasing T ($\propto \eta$), a trend expected from theory. Nystrom et. al. (1991) have shown, for a sol-gel transition caused by heating rather than cooling, the number of cross-links between polymer chains must increase as T is increased. Therefore, ξ must **decrease** via heating, as the cross-link density increases and their average separation decreases. For PAAA, the opposite is true - ξ must **increase** via heating, as cross-links are broken, and the network breaks down, i.e. the trend in figure 4.2.7 is reversed for sol-gel transitions induced through heating. As T is decreased, the gelation phase is approached, and the length scale characterising the correlation between neighbouring cross-links thus increases. Again, these length

scales are difficult to compute for the slow mode due to the complexity of the dynamics.

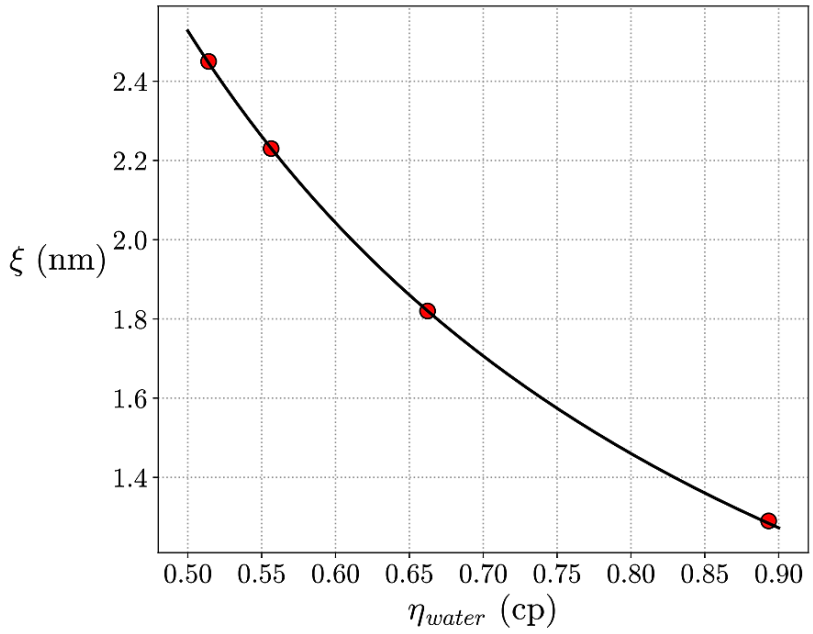

Figure 4.2.7. Characteristic length scale variation with solution viscosity. Temperature decrease is left-right and temperature increase is right-left. The fit is a power-law, $\xi \propto \eta^{-\alpha}$ with $\alpha = 1.17$. ξ is calculated using equation 2.3.8, with D calculated from the red line average fit in figure 4.2.5.

A significant problem was encountered early in the stretched exponential fitting procedure, although only with regards to the fast mode. As mentioned in section 3.2, linearised profiles of g_1 were used to provide an initial estimate for the stretching parameter, β. For the slow mode, this worked remarkably well and the estimate for β almost always matched closely with the β value obtained from the fitting parameters. For the fast mode however, the two values of β were almost always uncorrelated. This is demonstrated in tables 4.2.2 and 4.2.3. The accuracies in estimates for β are taken from the least squares fitting procedure.

Concentration (wt%)	T(K)	$\langle\beta\rangle_{\text{fast}}$ from log-log plot	$\langle\beta\rangle_{\text{fast}}$ from fitting	$\langle\beta\rangle_{\text{fast}}^{(\text{log})} / \langle\beta\rangle_{\text{fast}}^{(\text{fit})}$
1.09%	298	0.71	0.90	0.79
	330	0.62	0.94	0.66
1.11% (sample 1)	298	0.85	0.92	0.92
	312	0.83	0.90	0.92
	322	0.76	0.90	0.84
	327	0.73	0.81	0.90
1.11% (sample 2)	298	0.76	0.77	0.99
	316	0.74	0.86	0.86
	322	0.70	0.96	0.73
	327.1	0.71	0.80	0.89
3.79%	346.7	0.59	0.91	0.65
	353.4	0.56	0.83	0.67

Table 4.2.1. Fast mode stretching parameters from the linearised plots vs the parameters obtained from the fitting programs for three concentrations and various temperatures – averaged over all q in each q-run (0.75% and 2.14% datasets only contain T-runs, hence their omission here). The ratio between each β shown in the last column.

Concentration (wt%)	T(K)	$\langle\beta\rangle_{slow}$ from log-log	$\langle\beta\rangle_{slow}$ from fitting	$\langle\beta\rangle_{slow}^{(log)} / \langle\beta\rangle_{slow}^{(fit)}$
1.09%	298	0.28	0.28	1.01
	330	0.64	0.75	0.85
1.11% (sample 1)	298	0.28	0.28	1.01
	312	0.28	0.28	1.00
	322	0.30	0.30	1.00
	327	0.43	0.43	1.00
1.11% (sample 2)	298	0.26	0.27	0.96
	316	0.28	0.27	1.04
	322	0.29	0.27	1.07
	327.1	0.41	0.38	1.07
3.79%	346.7	0.65	0.75	0.97
	353.4	0.68	0.69	1.01

Table 4.2.2. Slow mode stretching parameters from the linearised plots vs the parameters obtained from the fitting programs for three concentrations and various temperatures – averaged over all q in each q-run (0.75% and 2.14% datasets only contain T-runs, hence their omission here). The ratio between each β shown in the last column.

In tables 4.2.2 and 4.2.3, notice the large variation in β from the log-log plots for the fast relaxation, while there is minimal variation for the slow relaxation, later confirmed to be a result of the fitting procedures. More specifically, consider $g_1 = A\exp\left[-(t/\tau)^{\beta}\right] + B$ with $B = 1 - A$, and the same function with A and B left as free parameters. This is demonstrated in figure 4.2.8.

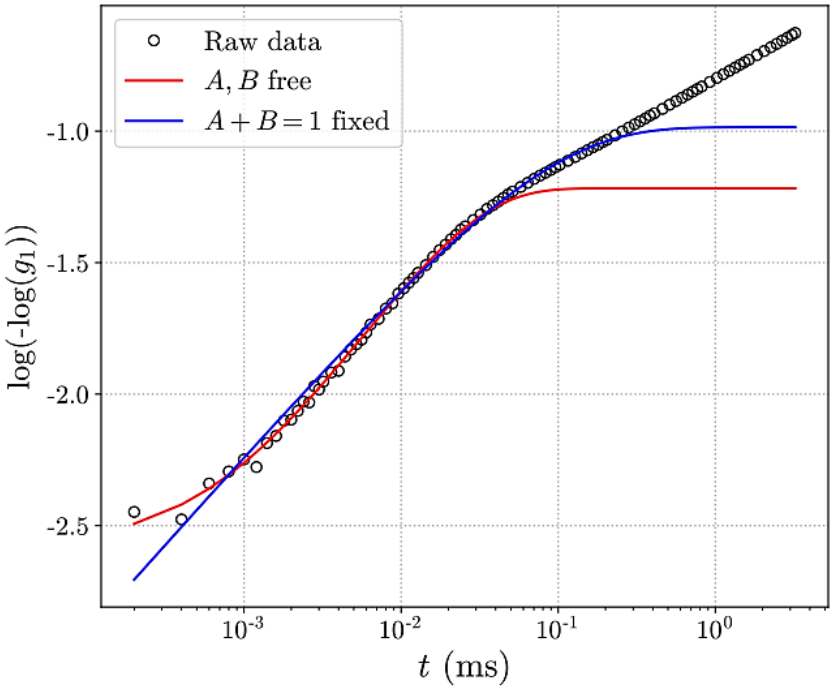

Figure 4.2.8. Fast mode raw data (1.11%, 60°,327K) linearised by taking logarithms twice, with fits. The red line is a fit of $g_1 = A\exp\left[-(t/\tau)^{\beta}\right] + B$ while the blue line is a fit of $g_1 = A\exp\left[-(t/\tau)^{\beta}\right] + (1 - A)$. The red fit has $A = 0.12$, $\boldsymbol{\beta} = \mathbf{0.96}$, $\tau = 0.02$ms, $B = 0.87$ and the blue fit has $A = 0.21$, $\boldsymbol{\beta} = \mathbf{0.67}$, $\tau = 0.06$ms.

Predicted from theory, the gradient of the lines in figure 4.2.9 should correspond to β for the fast mode, although clearly this is not the case here, as the β fitting parameters are significantly different for each function. This behaviour was observed in stretched exponential fits to the fast mode for all data sets. Although

theoretically $A + B$ should equal 1, fits seemed to converge far more successfully if A and B were left free (i.e. the red line in figure 4.2.8 was a better description of the fast mode). Therefore, the method of estimating β using the linearised data such as in figure 4.2.8 was not viable for the fast mode. Importantly, for the fast mode, β appeared to cluster around an average value for all q, suggesting the stretched behaviour is similar on all length scales, but this is not the case for the slow mode, in general, β_{slow} decreased with increasing q. The averages taken in table 4.2.2. β_{slow} are purely for demonstrative purposes, to argue for the log-log method's viability of estimating β.

Trends differed between q-runs at different concentrations and temperatures, as shown in figure 4.2.9.

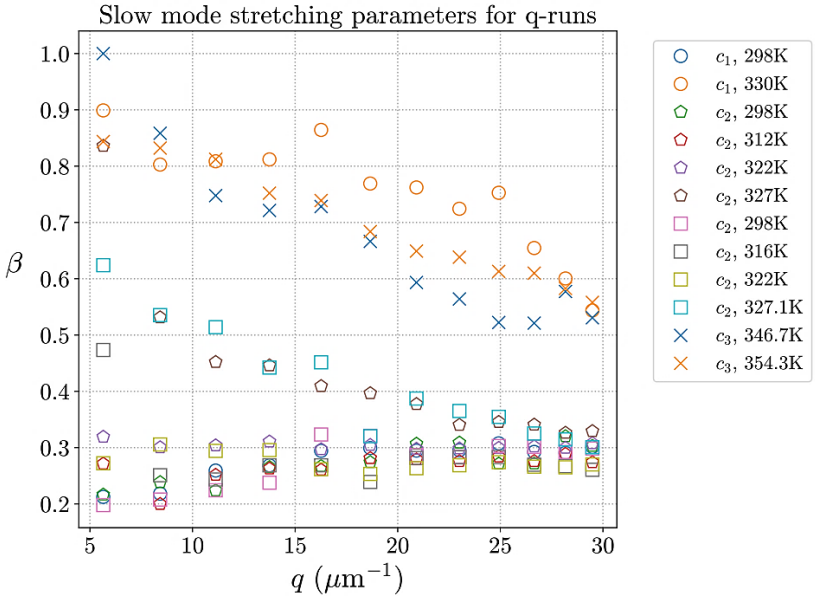

Figure 4.2.9. Slow mode stretching parameters for three concentrations, $c_1 = 1.09\%$, $c_2 = 1.11\%$ and $c_3 = 3.79\%$. The shapes group together the different samples (e.g. pentagons and squares have the same concentration but are separately prepared samples).

For higher temperatures, the slow mode is less stretched, as β remains high. As the scattering angle is increased, the probed length scale decreases, and β appears to decrease: the decay broadens and becomes more stretched. As the temperature is decreased below $\sim 322\text{K}$, the average value of β decreases, and stabilises as the solution enters the gel phase. This occurs at around $\beta = 0.2 - 0.3$, significantly more stretched than the fast mode, although there is still some fluctuation around this value. Changing the probed length scale in the gel state is observed to have minimal effect in the stretching parameter demonstrated by the $\sim$ flat curves for lower temperatures.

4.3 Analysis of τ_{slow} and the gelation transitions

An analysis of the slow relaxation for T-runs for all concentrations was performed to study the gelation transition in comparison to the glass transition in glassy systems. The average characteristic decay times of the slow mode and the viscosity of the sample ($\eta = \eta_{\text{water}} + \eta_{\text{PAAA}}$) should diverge upon approaching the gel transition temperature. Hence, τ_{slow} is studied in this section. Common to all samples was a critical increase in the relaxation time upon approaching some temperature, defined T_c. For glass forming systems, the glass transition is usually defined as the point at which relaxation times are of the order $100s$. However, for this system, the relaxation times rarely exceeded $5s$. Nonetheless, analytical fits of the Vogel-Fulcher-Tammann (VFT) relation [46,47] were used to estimate the critical temperatures. The VFT equation is an exponential increase in τ, during which an energy barrier is broken as a glass is formed [46,47]. Modelling the gel transition as a weak glass transition,

$$\langle \tau \rangle = \tau_0 \exp\left(\frac{A}{T - T_0}\right) = \tau_0 \exp\left(\frac{E_A(T)}{kT}\right) \tag{4.3.1}$$

where A is a constant with units of temperature, τ_0 is a characteristic time scale and $E_A(T)$ is a temperature-dependent energy barrier. T_0 is an extrapolated divergent temperature, not necessarily the gelation temperature. As shown in figure 4.3.1, critical temperatures increase as a function of the concentration of polymer in water.

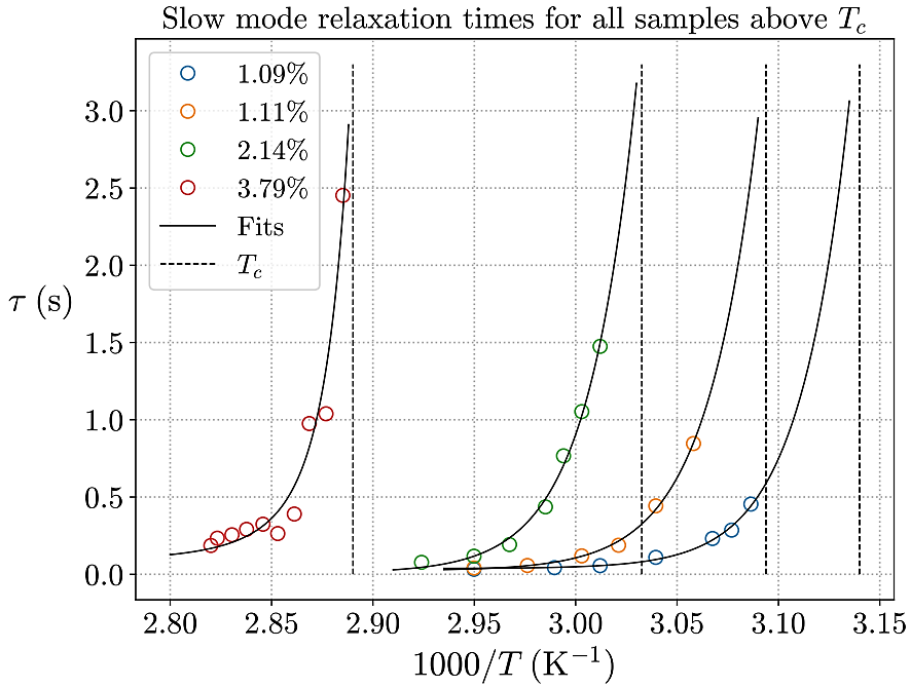

Figure 4.3.1. Growth in relaxation times as a function of inverse temperature (left-right is cooling, and right-left is heating). Fits are from equation 4.3.1 (Arrhenius plot) and the dotted lines represent the critical temperatures. 0.75% is not pictured here as the relaxation times are too small to be visible at this scale. Typically plotted logarithmically in τ, although this introduces visibility problems for some data points if performed here, so the vertical axis is left linear.

Figure 4.3.2 shows the approximately linear relationship between T_c and c. All relaxation times are those taken towards the higher end of the temperature range.

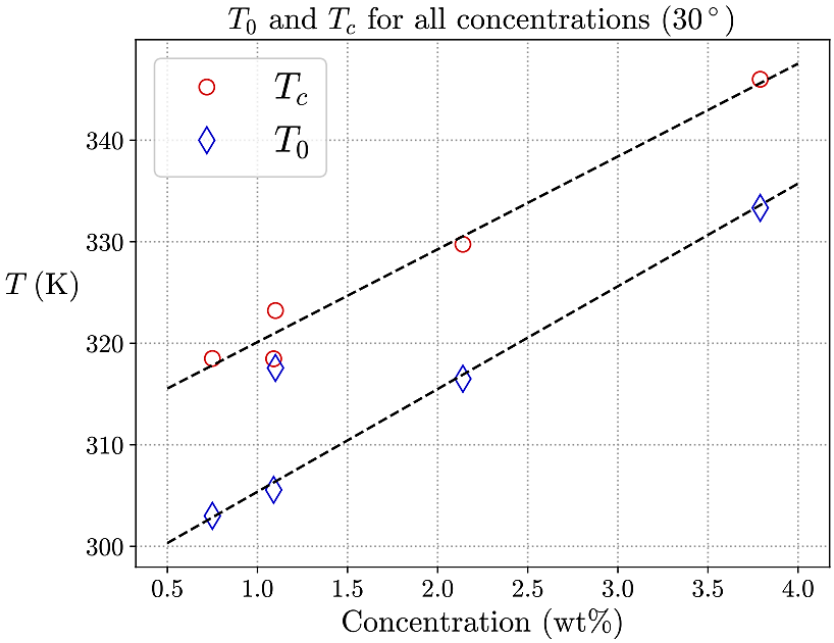

Figure 4.3.2. Variation of the divergent temperature, T_0, and the critical temperature, T_c, as a function of the concentration of PAAA in water. Divergent temperatures are estimated from equation 4.3.1 and critical temperatures from equation 4.3.2. Linear fit to T_0 has gradient 10.1 while to T_c has gradient 9.1.

If the whole range of τ is plotted, the reality of the transition is revealed – $\langle\tau\rangle$ converges to a finite peak and then drops again past the critical temperature. This suggests that relaxations become slower as the temperature is **increased** while in the **gel state** and relaxations become slower as the temperature is **decreased** in the **sol state**. Perhaps this is an indication of the switch in dynamics which produces the slow mode. This is demonstrated for one sample in figure 4.3.3.

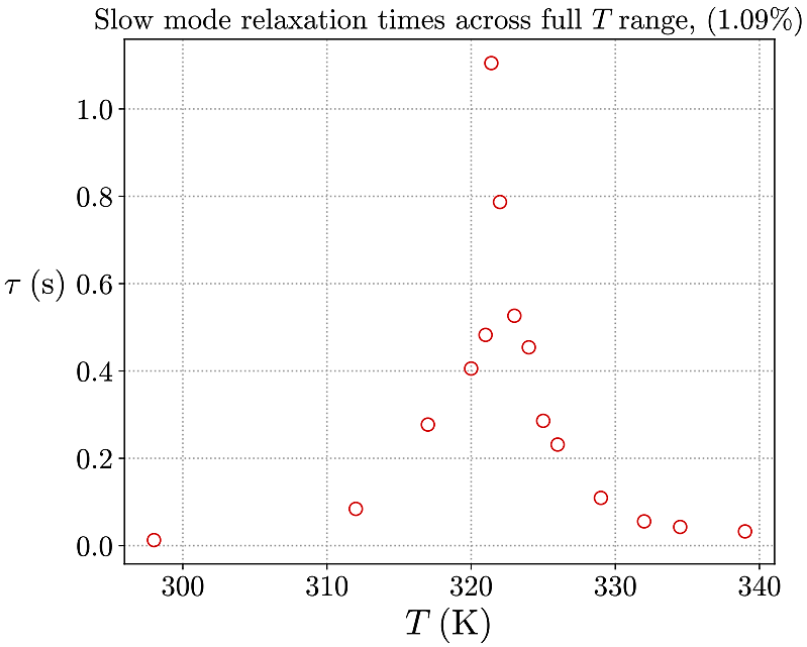

Figure 4.3.3. Slow mode relaxation times across the full temperature range for one sample (1.09%).

The range of relaxation times shown in figures 4.3.1/4.3.3 are not indicative of a glass-like transition, however, as $\langle\tau\rangle \ll 100s$ for all samples. The relationship between $\langle\tau\rangle$ and $(T - T_c)/T_c$ is also studied in glassy systems, often taking the form of a power-law:

$$\langle\tau\rangle = \tau_1 \left(\frac{T - T_c}{T_c}\right)^{-\gamma}, \tag{4.3.2}$$

where $\gamma > 0$ [46]. The results of linear fits to each set of data are shown in figure 4.3.4.

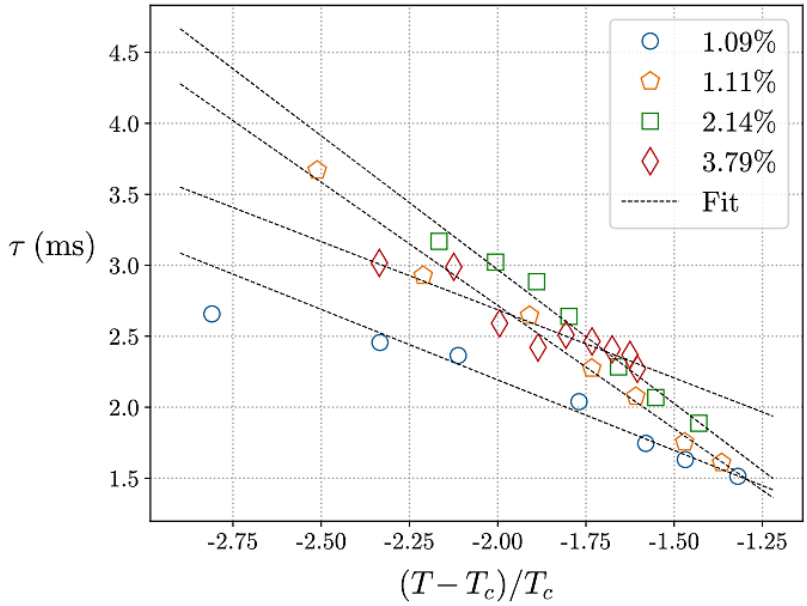

Figure 4.3.4. Slow mode relaxation times as a function of reduced temperature for temperatures greater than T_c in a log-log plot. Linear fits are representative of power-laws of the form shown in equation 4.3.3.

The discrepancy between T_0 and T_c is shown in figure 4.3.2 and is expected. T_0 is not a physical transition temperature, it is a mathematical *divergent* temperature, where $\langle\tau\rangle, \eta \to \infty$. The difference between $T_c - T_0 \sim 12\text{K}$ appears to be consistent across all samples, and $T_0 < T_c$ is expected from the VFT equation, however the 1.11% sample appears not to follow this trend, as $T_0 \approx T_c$. This is most likely due to the fitting procedures used, as some problems were encountered in finding non-degenerate fits. In section 4.1 it was predicted that $T_{c,0.75} \sim 310\text{K}$, $T_{c,1.11} \sim 327\text{K}$ and $T_{c,3.79} \sim 347\text{K}$, supported by results shown in figure 4.3.2, within margins of error. This is attributed to the ambiguity in where T_c should be placed on the spectrum of τ (see figure 4.3.3 – there is a variation in where one may consider the transition occurs). There appears to be no discernible relationship between the value of γ and the concentration, c. The change in the stretching parameter, β with the ratio $\langle\tau\rangle/\tau_1$ is shown in figure 4.3.5.

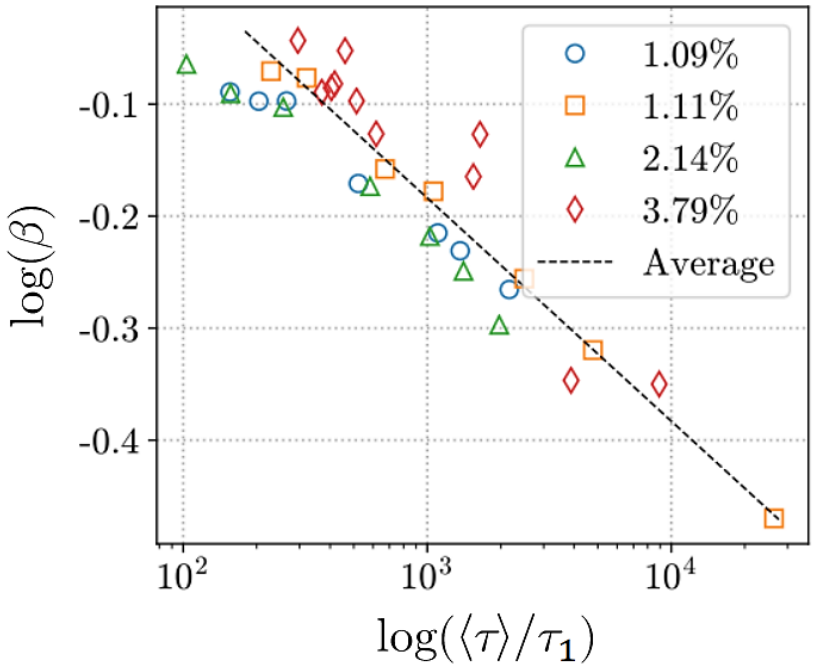

Figure 4.3.5. Slow mode stretching parameters for $T > T_c$. The linear fits average well to a single slope for all data, indicating a power-law relationship between β and τ/τ_1. τ_1 is the characteristic timescale from the fits to equation 4.3.2. The slope of the line is -0.2.

Figure 4.3.5 suggests that a critical **increase** in $\langle\tau\rangle$ towards the gelation temperature is closely associated with a critical **decrease** in the stretching parameter, β. β varies from ~ 0.8 towards ~ 0.3 as relaxations are slowed and the sample enters the gel phase. This is commonly seen in both gels and glasses [46,48]. This trend is also seen in section 4.1, figure 4.1.6, as β increases via sample heating.

4.4 Fits to the full domain of g_1

It is commonly reported in literature that the slow mode in non-ergodic (i.e. gel) systems is suppressed, and a stretched exponential is not used [39]. However, in this study, the stretched exponential fitting was performed for all systems, ergodic or not. This found some success, and some of the previous results discussed in section 4.3, such as τ_{slow} for each sample, were obtained from stretched fitting. Figure 4.4.1 shows one result of the fits to equation 3.3.1, for the 1.11% sample at the lowest temperature. The function fits well to the data, although it can be said that other functions appear to fit well as well, despite this, observing other functional fits showed equation 3.3.1 was the best fit. The fitting parameters were generated from a logarithmic plot of just the intermediate regime, which gave an estimate for the exponent α. Figure 4.4.2 is a

demonstration of an ergodic set of data with fits to equation 3.3.1. Notice, however, that the fit in figure 4.4.2 is more uncorrelated with the data than in figure 4.4.1.

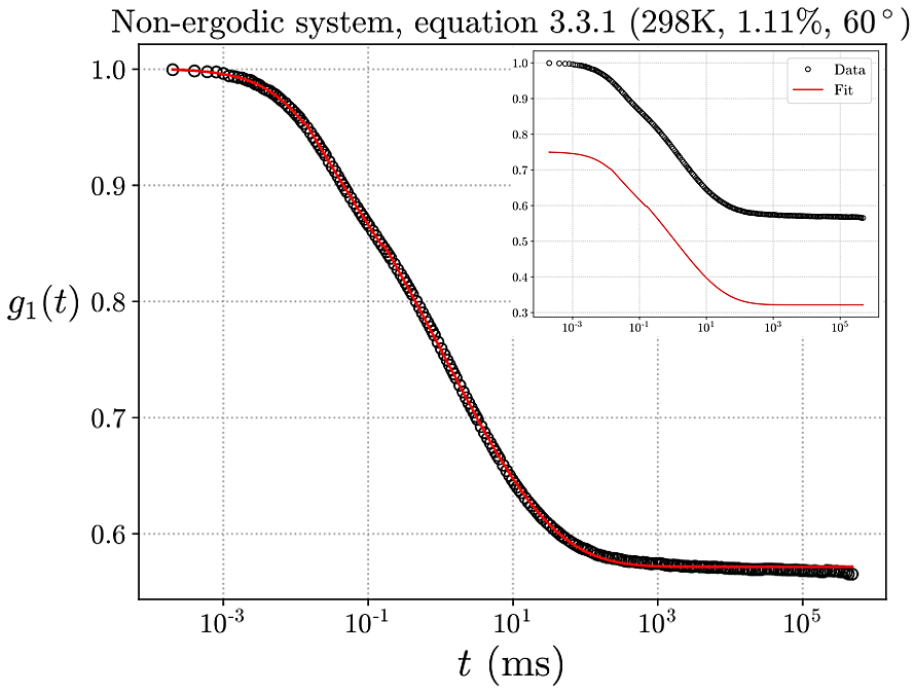

Figure 4.4.1. Calculated g_1 data for a non-ergodic set of data from the 1.11% concentration sample. $\theta = 60°$ and $T = 298\text{K}$. The red line is a fit to equation 3.3.1, two stretched exponentials and a power-law for the intermediate regime. The inset plot is for clarity, to compare the shapes of the fit and the raw data. Note g_1 does not decay to zero, rather ≈ 0.58, a consequence of the strong cross-links formed between polymer chains at this temperature.

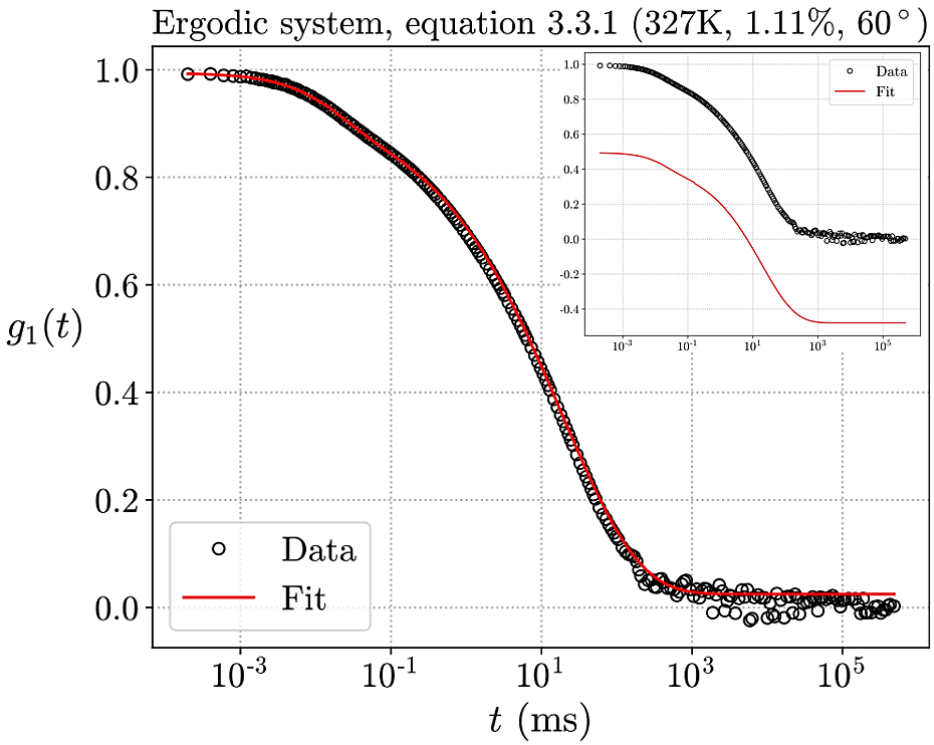

Figure 4.4.2. Calculated g_1 data for an ergodic set of data from the 1.11% concentration sample. $\theta = 60°$ and $T = 327\text{K}$. The red line is a fit to equation 3.3.1, two stretched exponentials and a power-law for the intermediate regime. The inset plot is for clarity, to compare the shapes of the fit and the raw data. Note g_1 does not decay to zero, rather ≈ 0.01, a result of the noise at large t.

This procedure was repeated for the remaining temperatures of the 1.11% sample and the results for α are shown in semi-log plot in figure 4.4.3, demonstrating that the power-law may not be T-dependent for constant

c and q as the data seem to converge closely to the average linear fit. In addition to this, a linear plot of α vs q appears logarithmic, because figure 4.4.3 predicts $\alpha \propto \log(q)$:

$$\alpha = -k\log(q) + C \tag{4.4.1}$$

for the intermediate regime, where $k > 0$ and $C > 0$ are constants. Figures 4.4.3 and 4.4.4 show these relationships.

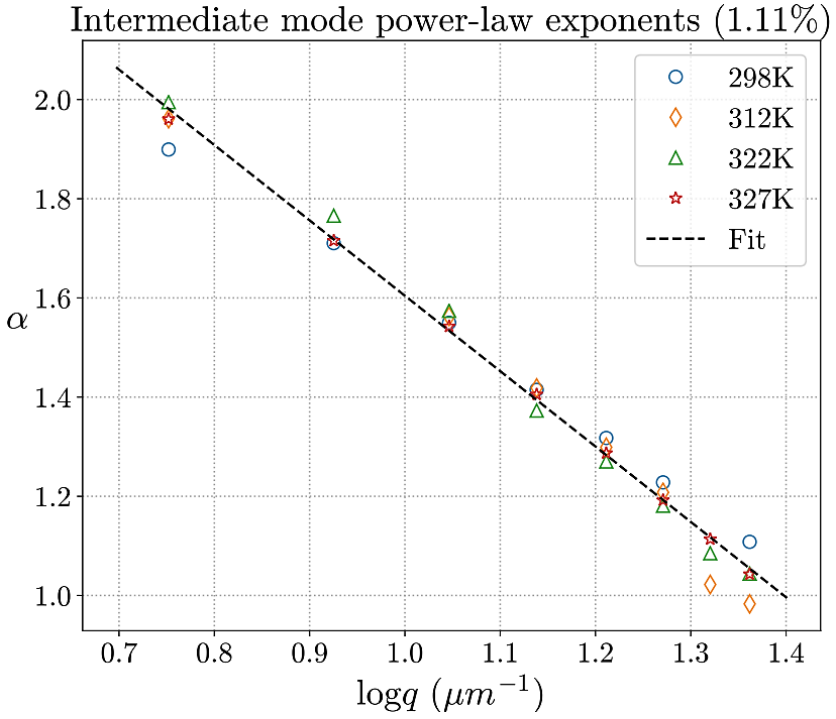

Figure 4.4.3. Semi logarithmic plot of α and q corresponding to the second term in equation 3.3.1, for all temperatures of the 1.11% sample. The dotted line is an average fit with gradient -1.5 ± 0.2 where the error is estimated from the spread of values.

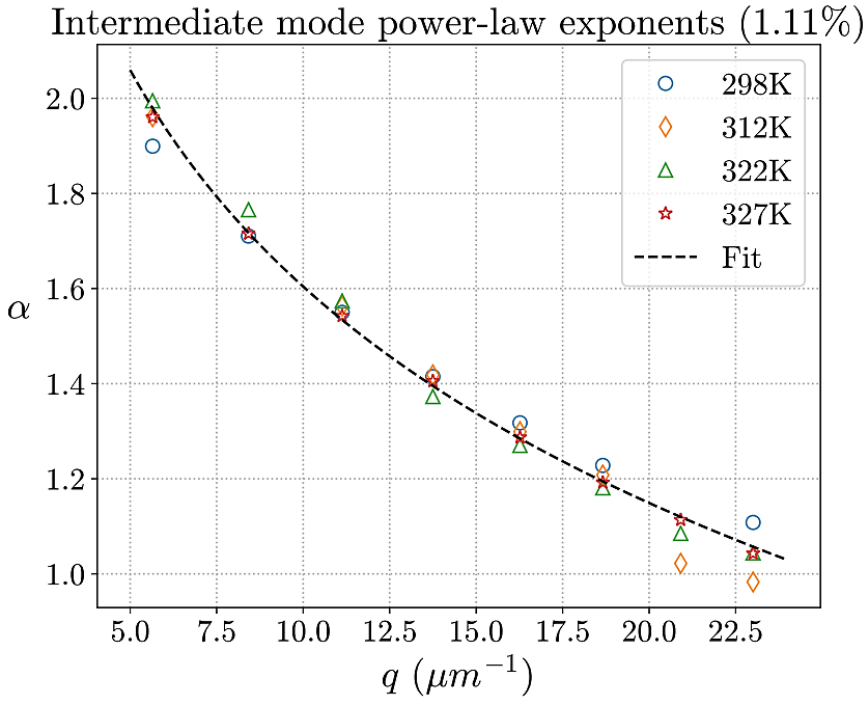

Figure 4.4.4. Linear plot of α and q corresponding to the second term in equation 3.3.1, for all temperatures of the 1.11% sample. The dotted line is an average fit of equation 4.4.1 with $k = 1.5 \pm 0.2$ and $C = 3.1 \pm 0.1$ where the errors are estimated from the spread of fit parameters.

This is equally well interpreted as $q \sim \exp(\alpha/k)$. This form and the form in equation 4.4.1 are perhaps not entirely useful, as it is simpler to just use $t^{-\alpha}$. Nonetheless, this relation gives some insight into the physical significance of the power-law exponent, α. Note, however, the linear fit is only approximate, as all data sets appear to deviate above/below the fit for lower q and below/above the fit for higher q. This suggests a linear fit in the exponents α may not be appropriate.

Fitting with equation 3.3.4 was attempted for some datasets, although was largely unsuccessful. An example of a successful fit is shown in figure 4.4.5.

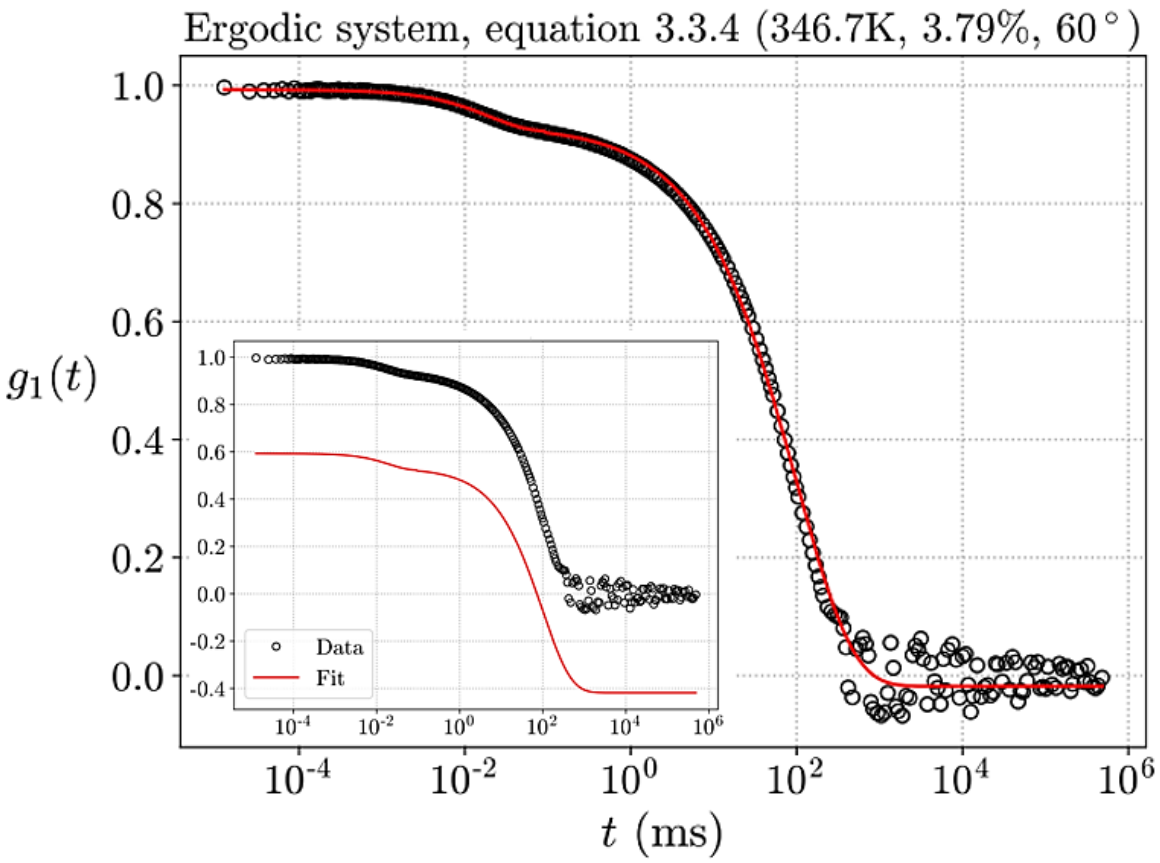

Figure 4.4.5. Calculated g_1 data for an ergodic set of data from the 3.79% concentration sample. $\theta = 60°$ and $T = 346.7\text{K}$. The red line is a spliced fit to equation 3.3.4, $A\exp[b(1-\exp(-(t/\tau)^{\beta})]$ for the fast and intermediate regimes together, and a stretched exponential for the slow mode. The inset plot is for clarity, to compare the shapes of the fit and the raw data. Note g_1 does not decay to zero, rather ≈ -0.07, a consequence of noise.

Therefore, the form used to fit the fast and intermediate modes is deemed experimental, and not a representation of the true dynamics of the system. To assess the concentration dependence on the intermediate region, the size and breadth of the region is compared for relatively low and high concentrations in figure 4.4.6. Despite the mismatch in temperatures, this comparison can be made for any $T > T_c$ and the same change in intermediate region size can be observed for both. The curved region in between the two linear regions is indicative of the deviation from exponential or stretched exponential behaviour (otherwise $\log(-\log(g1))$ would be linear), indicating some different dynamics are present for this region. This region grows substantially with increasing concentration, as the intermediate mode becomes more significant. Perhaps this can be described using a power-law as outline above, although it could be another function that has not been considered in this study.

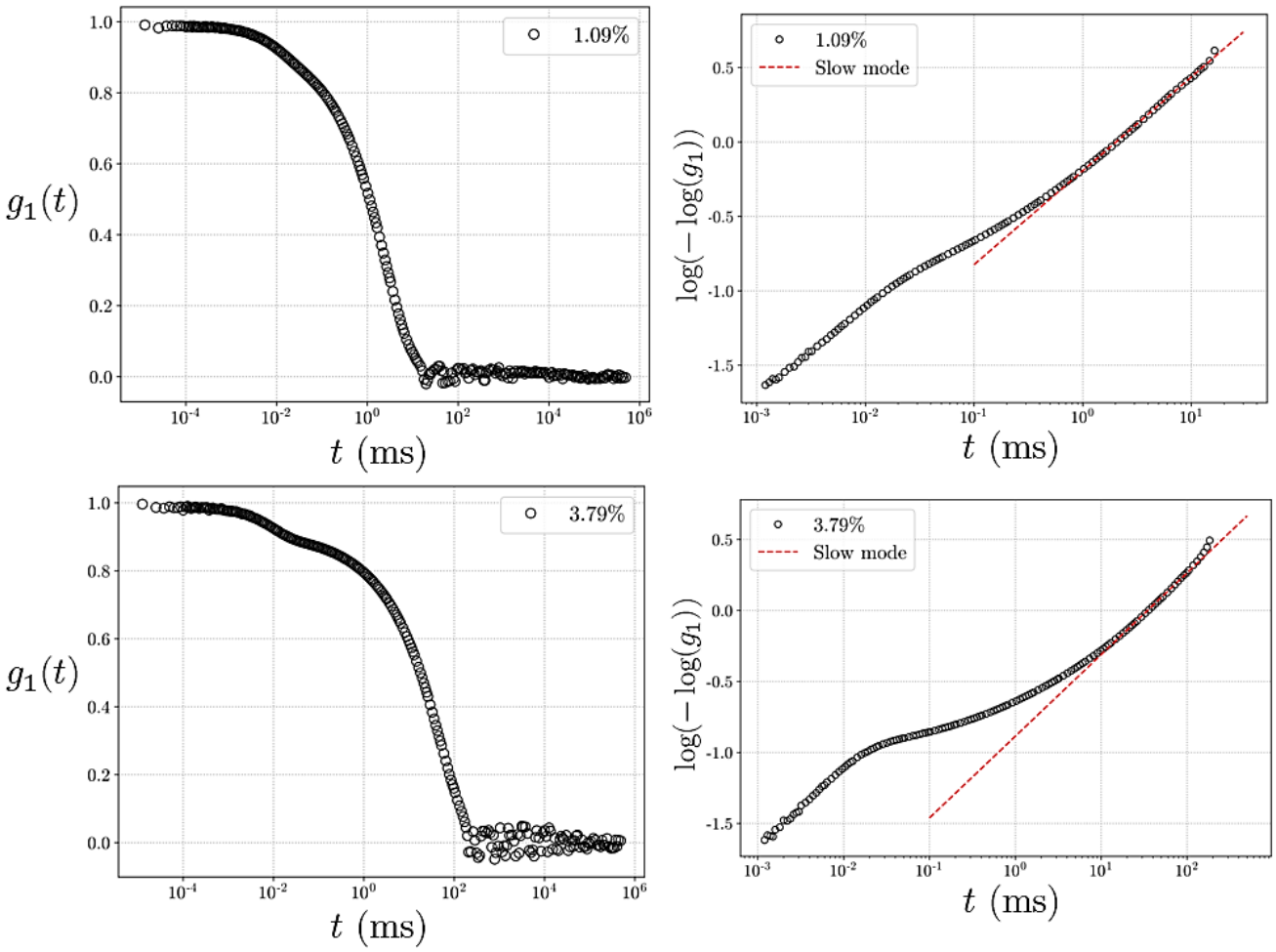

Figure 4.4.6. g_1 for two concentrations, 1.09% and 3.79% for temperatures $T = 330\text{K}$ and $T = 346.7\text{K}$ respectively (both greater than T_c). Both curves are from data sets with $\theta = 80°$. The right-hand plots are plots of $\log(-\log(g1))$ vs t, and the red dotted lines are linear fits to the slow relaxation, with gradients β_{slow}.

5 Conclusions and future work

Dynamic light scattering (DLS) is an important tool for probing the sizes and dynamics of microstructures. Typically applied to a range of systems, this technique can provide a broad picture of the properties of a material when combined with other techniques such as rheology. This study considered the analysis of autocorrelation data recorded from DLS experiments with poly(N-acetamido acrylamide) (PAAA) hydrogels. Analysis of the decays of scattered light intensity fluctuations provided an indirect measurement of the density fluctuations of PAAA systems of various concentrations in water. DLS experiments calculate the intensity autocorrelation function (ACF), g_2, comparing count-rate measurements separated by a lag time, t. The ergodicity of each system was analysed: whether ensemble ($\langle I \rangle_E$) and temporal ($\langle I \rangle_T$) averages are equivalent. It is well known that polymer gels are non-ergodic, whilst in the sol phase they can be considered ergodic. The ergodicity was determined through observation ($g_2 - 1 \to 0$) or through direct computation of $Y = \langle I \rangle_E / \langle I \rangle_T$. The electric field ACF, g_1, was then directly determined from g_2 using the value of Y. Y was found to lie close to 1 for data sets which appeared ergodic, proving it as a reliable measure of ergodicity.

g_1 data was analysed for PAAA concentrations ranging from 0.75wt% to 3.79wt%, to determine the effect of concentration on the sol-gel transition. Measurements were taken through variation of the angular position of the detector, q-runs (q = scattering wave vector), and temperature, T-runs. g_1 curves changed shape (breadth, width) predictably with q and T, consistent with what was expected from previous studies of gel

systems. Stretched exponential was performed, to develop a model of the motions within the gel samples. The fast relaxations, $t \sim 0.001\text{ms} - 1\text{ms}$, were predicted to be a result of cooperative diffusion of polymer chains, obeying Brownian motion/random walks. This was demonstrated by analysing the relationship between τ and q: $\tau \sim q^{-2}$ was found for most sets of data. For the slowest relaxations, $t \sim 5\text{ms} - 1\text{s}$, the exponent γ in $\tau \sim q^{-\gamma}$ was found to vary significantly, indicating there may be a vast range of different dynamics, such as the motions of cross-links and reptation, which cause the density fluctuations seen as the slow mode. τ was observed to critically increase as the sample approached a critical temperature, T_c, predicted to be closely related to the sol-gel transition temperature. This temperature was further shown to vary approximately linearly with the concentration of polymer in solution. Collection of data with a more granular range of temperatures may be useful for improving these estimates of T_c. Additionally, a wider range of concentrations may be used to assess the changes in T_c, as well as τ and β.

An intermediate regime was seen frequently across many of the sets of data. This regime is less frequently reported in literature, although stretched-exponential and power-law behaviours have been suggested. A variety of methods were employed for analysis of this mode, power-law fits being the most successful. The power-law exponents, α, were shown to vary logarithmically with q, a relationship of possible use in future analyses. In general, more success was found in analytical fitting to all three regimes using a spliced function – separate functions applying to each mode – as opposed to a sum of three functions. For example, the power-law decay was deemed inappropriate for fitting to the fast and slow regimes, as it incorrectly represents the dynamics of these modes.

Future work should place more focus on descriptions and models for the intermediate and slow regimes. The fast mode is well understood, explained by cooperative diffusion of polymer chains, while the intermediate and slow modes are not universally explained. Untested in this study is the collapsing of the slow mode across a q-run; scaling of the t axis with q^{γ} for $\gamma = 3{,}4{,}5$ etc should be attempted to develop a model for the dynamics which produce the slow mode. If successful, a more complete description of the dynamics can be formulated. Similarly, the intermediate mode is not well understood, although is possibly connected to the fast mode. For example, this study has shown collapsing of the fast *and* intermediate modes together, suggesting the intermediate mode may be diffusive. However, the scaling procedure was not attempted for sets of data with large intermediate regimes. In addition to this, the fast and slow modes are well described by stretched exponentials, whereas the intermediate mode can be modelled with a range of functions. This is attributed to the relative insignificance of the relaxation in most data sets. Therefore, attempts should be made to grow this mode in g_1 data by focusing on a set of conditions which are known to produce a large intermediate mode. A large range of data using these conditions may be statistically useful for analysing this mode. As mentioned in section 3.3, to find non-degenerate fits to the entire decay profile of g_1 one must relate the stretching parameters and characteristic time scales of the fast and intermediate mode. This is predicted to be possible as these modes appear closely related, while the slow mode is described by fundamentally different dynamics. If the number of parameters can be reduced, so can the number of unique fits – more accurately describing the entire decay. This study has demonstrated the degeneracy of fits, many choices of parameters can be chosen to fit closely to the data. In addition to this, many choices and combinations of functions can fit autocorrelation data successfully.

As a general improvement for the analysis of PAAA hydrogels, static light scattering (SLS) data should be analysed. This can provide essential information to support the conclusions of this study using DLS data, for example, the model of gelation may be improved if the physical form of the polymer networks can be determined, such as estimating the fractal dimension from SLS. Furthermore, the majority of the data was recorded when PAAA was in the sol state – perhaps a larger selection of data for $T < T_c$ will improve on the models proposed in this study.

6 References

[1] Kleman, M., 2003. *Soft Matter Physics - An Introduction*. New York, NY: Springer.

[2] Pecora, R., 2013. *Dynamic Light Scattering*. New York, NY: Springer.

[3] Dasgupta, B., 2004. *Microrheology and Dynamic Light Scattering Studies of Polymer Solutions*. Ph.D. Harvard University.

[4] Martin, J. and Adolf, D., 1991. The Sol-Gel Transition in Chemical Gels. *Annual Review of Physical Chemistry*, **42**(1), pp.311-339.

[5] Qiu, Y. and Park, K., 2001. Environment-sensitive hydrogels for drug delivery. *Advanced Drug Delivery Reviews*, **53**(3), pp.321-339.

[6] Zhong, Y. and Shultz, R., 2021. Hydrogel-based local drug delivery strategies for spinal cord repair. *Neural Regeneration Research*, **16**(2), p.247.

[7] Kjøniksen, A., Hiorth, M. and Nyström, B., 2004. Temperature-induced association and gelation of aqueous solutions of pectin. A dynamic light scattering study. *European Polymer Journal*, **40**(11), pp.2427-2435.

[8] Mateescu, A., Wang, Y., Dostalek, J. and Jonas, U., 2012. Thin Hydrogel Films for Optical Biosensor Applications. *Membranes*, **2**(1), pp.40-69.

[9] Martin, J. and Wilcoxon, J., 1988. Critical Dynamics of the Sol-Gel Transition. *Physical Review Letters*, **61**(3), pp.373-376.

[10] Marstokk, O., Nyström, B. and Roots, J., 1998. Effect of Denaturant and Polymer Concentration on the Structural and Dynamical Properties of Aqueous Solutions of Poly(N-acetamido acrylamide). *Macromolecules*, **31**(13), pp.4205-4212.

[11] Jeraldo, P., 2005. Critical Phenomena in Percolation Theory.

[12] Li, X., Nakagawa, S., Tsuji, Y., Watanabe, N. and Shibayama, M., 2019. Polymer gel with a flexible and highly ordered three-dimensional network synthesized via bond percolation. *Science Advances*, **5**(12), p.eaax8647.

[13] Strelniker, Y.M., Havlin, S., Bunde A., 2009. Fractals and Percolation. In: Meyers R. (eds) Encyclopedia of Complexity and Systems Science. Springer, New York, NY. https://doi.org/10.1007/978-0-387-30440-3_227

[14] Mauro, J. and Mauro, Y., 2018. On the Prony series representation of stretched exponential relaxation. *Physica A: Statistical Mechanics and its Applications*, **506**, pp.75-87.

[15] Kjøniksen, A., Hiorth, M., Roots, J. and Nyström, B., 2003. Shear-Induced Association and Gelation of Aqueous Solutions of Pectin. *The Journal of Physical Chemistry B*, **107**(26), pp.6324-6328.

[16] Joosten, J., McCarthy, J. and Pusey, P., 1991. Dynamic and static light scattering by aqueous polyacrylamide gels. *Macromolecules*, **24**(25), pp.6690-6699.

[17] Sakai, T., 2020. *Physics of polymer gels*. Weinheim: Wiley-VCH.

[18] Fahimi, Z., Aangenendt, F., Voudouris, P., Mattsson, J. and Wyss, H., 2017. Diffusing-wave spectroscopy in a standard dynamic light scattering setup. *Physical Review E*, **96**(6).

[19] Nyström, B. and Lindman, B., 1995. Dynamic and Viscoelastic Properties during the Thermal Gelation Process of a Nonionic Cellulose Ether Dissolved in Water in the Presence of Ionic Surfactants. *Macromolecules*, 28(4), pp.967-974.

[20] Einaga, Y. and Karube, D., 1999. Analysis of the dynamic structure factor for semi-dilute solutions of polyisobutylene. *Polymer*, **40**(1), pp.157-169.

[21] Abe, M., 2019. *Measurement techniques and practices of colloid and interface phenomena*. Noda: Springer Nature Singapore Pte Ltd. Translation from the Japanese language edition: GENBA DE YAKUDATSU KOROIDO KAIMEN GENSHO NO SOKUTEI NOUHAU

[22] Löwe, H., Müller, P. and Zippelius, A., 2005. Rheology of gelling polymers in the Zimm model. *The Journal of Chemical Physics*, **122**(1), p.014905.

[23] King, T., 1989. Photon Correlation Spectroscopy: Technique and Scope. *Comprehensive Polymer Science and Supplements*, pp.911-935.

[24] De Gennes, P., 1976. Dynamics of Entangled Polymer Solutions. I. The Rouse Model. *Macromolecules*, **9**(4), pp.587-593.

[25] Mondal, M., 2017. Study of autocorrelation function of polymer and polymer–nanocomposite solutions using dynamic light scattering method. *Journal of Polymer Research*, **24**(12).

[26] Horkay, F., Hecht, A. and Geissler, E., 1994. Small Angle Neutron Scattering in Poly(vinyl alcohol) Hydrogels. *Macromolecules*, **27**(7), pp.1795-1798.

[27] Behra, J., Mattsson, J., Cayre, O., Robles, E., Tang, H. and Hunter, T., 2019. Characterization of Sodium Carboxymethyl Cellulose Aqueous Solutions to Support Complex Product Formulation: A Rheology and Light Scattering Study. *ACS Applied Polymer Materials*, **1**(3), pp.344-358.

[28] Okamoto, M., Norisuye, T. and Shibayama, M., 2001. Time-Resolved Dynamic Light Scattering Study on Gelation and Gel-Melting Processes of Gelatin Gels. *Macromolecules*, **34**(24), pp.8496-8502.

[29] Ostrovskii, D., Jacobsson, P., Nyström, B., Marstokk, O. and Kopperud, H., 1999. Raman Spectroscopic Characterization of Association and Thermoreversible Gelation in Aqueous Systems of Poly(N-acetamidoacrylamide). *Macromolecules*, **32**(17), pp.5552-5560.

[30] Lesturgeon, V., Nicolai, T. and Durand, D., 1999. Dynamic and static light scattering study of the formation of cross-linked PMMA gels. *The European Physical Journal B*, **9**(1), pp.71-82.

[31] Minton, A., 2016. Recent applications of light scattering measurement in the biological and biopharmaceutical sciences. *Analytical Biochemistry*, **501**, pp.4-22.

[32] Pusey, P. and Van Megen, W., 1989. Dynamic light scattering by non-ergodic media. *Physica A: Statistical Mechanics and its Applications*, **157**(2), pp.705-741.

[33] Nyström, B., Roots, J., Carlsson, A. and Lindman, B., 1992. Light scattering studies of the gelation process in an aqueous system of a non-ionic polymer and a cationic surfactant. *Polymer*, **33**(14), pp.2875-2882.

[34] Matsunaga, T. and Shibayama, M., 2007. Gel point determination of gelatin hydrogels by dynamic light scattering and rheological measurements. *Physical Review E*, **76**(3).

[35] Pham, K., Egelhaaf, S., Moussaïd, A. and Pusey, P., 2004. Ensemble-averaging in dynamic light scattering by an echo technique. *Review of Scientific Instruments*, **75**(7), pp.2419-2431.

[36] Kroon, M., Wegdam, G. and Sprik, R., 1996. Dynamic light scattering studies on the sol-gel transition of a suspension of anisotropic colloidal particles. *Physical Review E*, **54**(6), pp.6541-6550.

[37] Hansen, E., Gong, X. and Chen, Q., 2013. Compressed Exponential Response Function Arising From a Continuous Distribution of Gaussian Decays - Distribution Characteristics. *Macromolecular Chemistry and Physics*, **214**(7), pp.844-852.

[38] Gomes, C., Dias, R. and Costa, M., 2019. Static Light Scattering Monitoring and Kinetic Modeling of Polyacrylamide Hydrogel Synthesis. *Processes*, **7**(4), p.237.

[39] Wang, W. and Sande, S., 2014. A dynamic light scattering study of hydrogels with the addition of surfactant: a discussion of mesh size and correlation length. *Polymer Journal*, **47**(4), pp.302-310.

[40] Adam, M., Delsanti, M., Munch, J. and Durand, D., 1988. Dynamical Studies of Polymeric Cluster Solutions Obtained near the Gelation Threshold: Glasslike Behavior. *Physical Review Letters*, **61**(6), pp.706-709.

[41] Bordi, F., Paradossi, G., Rinaldi, C. and Ruzicka, B., 2002. Chemical and physical hydrogels: two casesystems studied by quasi elastic light scattering. *Physica A: Statistical Mechanics and its Applications*, **304**(1-2), pp.119-128.

[42] Teixeira, A., Geissler, E. and Licinio, P., 2007. Dynamic Scaling of Polymer Gels Comprising Nanoparticles. *The Journal of Physical Chemistry B*, **111**(2), pp.340-344.

[43] Shibayama, M. and Okamoto, M., 2001. Dynamic light scattering study on gelatin aqueous solutions and gels. *The Journal of Chemical Physics*, **115**(9), pp.4285-4291.

[44] Frisken, B., 2001. Revisiting the method of cumulants for the analysis of dynamic light-scattering data. *Applied Optics*, **40**(24), p.4087.

[45] Martin, J., Wilcoxon, J. and Odinek, J., 1991. Decay of density fluctuations in gels. *Physical Review A*, **43**(2), pp.858-872.

[46] Phan, A., Wakabayashi, K., Paluch, M. and Lam, V., 2019. Effects of cooling rate on structural relaxation in amorphous drugs: elastically collective nonlinear langevin equation theory and machine learning study. *RSC Advances*, **9**(69), pp.40214-40221.

[47] Svanberg, C., Adebahr, J., Ericson, H., Börjesson, L., Torell, L. and Scrosati, B., 1999. Diffusive and segmental dynamics in polymer gel electrolytes. *The Journal of Chemical Physics*, **111**(24), pp.11216-11221.

[48] Cardona, M., Chamberlin, R. and Marx, W., 2007. The history of the stretched exponential function. *Annalen der Physik*, **16**(12), pp.842-845.

7 Appendix

7.1 Brownian motion of uniform spheres

Brownian motion is characterised by random walks, particles randomly choosing a direction at each time step. The particle density is given by

$$\rho(\vec{r},t)=\sum_{i=1}^{N}\delta(\vec{r}-\vec{r_i}(t)) \tag{7.1.1}$$

where $\vec{r}$ is the final position, $\vec{r_i}(t)$ is the time-dependent position of the i^{th} particle and δ denotes the Dirac delta function. The delta function for uniform spheres is 1 where there exists a particle, and 0 where there is no particle, such that if $\vec{r_i}(t)=\vec{r}$, there is a contribution to $\rho(\vec{r},t)$ from that particle. The Van Hove correlation function correlates the positions of a pair of particles at $\vec{r}=0$ and $\vec{r}=\vec{r}$ at times $t=0$ and $t=t$:

$$g(\vec{r},t)=\frac{1}{\rho_0}\langle\rho(0,0)\cdot\rho(\vec{r},t)\rangle \tag{7.1.2}$$

where ρ_0 is a characteristic particle density. The intermediate scattering function is defined as the Fourier transform of $g(\vec{r},t)$:

$$S(\vec{q},t)=\int g(\vec{r},t)e^{i(\vec{q}\cdot\vec{r})}d\vec{r} \tag{7.1.3}$$

where the scattering vector, $\vec{q}$, represents momentum space and $S(\vec{q},t)$ is directly proportional to g_1.

$$g_1(t)=\frac{S(\vec{q},t)}{S(\vec{q},0)} \tag{7.1.4}$$

True randomness is described by a Gaussian probability distribution of the 1D displacements. In 1D, suppose one jump is made of length x_0 for every unit of time, such that $\langle x^2\rangle = N{x_0}^2$ for N steps. Assuming N must be even, the diffusion coefficient is defined as $D=N{x_0}^2/2t$ as the interval between jumps is twice the time for one jump, therefore, $\langle x^2\rangle = 2Dt$.

$$g(x,t)\sim\exp\left[-\frac{1}{2}\frac{(x-\bar{x})^2}{\sigma^2}\right]=\exp\left[-\frac{1}{4}\frac{x^2}{Dt}\right]=\exp\left[-\frac{1}{2}\frac{x^2}{\langle x^2\rangle}\right] \tag{7.1.5}$$

Where $\bar{x}$ is the mean displacement, equal to zero as the distribution does not favour one specific direction, and σ^2 is the variance from the mean, equal to the mean-squared displacement. For three dimensions,

$$g(r,t) \sim \exp\left[-\frac{1}{4}\frac{r^2}{Dt}\right] = \exp\left[-\frac{3}{2}\frac{r^2}{\langle \Delta r^2(t)\rangle}\right] \tag{7.1.6}$$

where the factor of 3 comes from the 3 spatial dimensions so $\langle \Delta r^2(t)\rangle = 6Dt$. The intermediate scattering function is then:

$$S(q,t) = \int \exp\left[-\frac{3}{2}\frac{r^2}{\langle \Delta r^2(t)\rangle}\right] \cdot e^{i(\vec{q}\cdot\vec{r})} dr \tag{7.1.7a}$$

$$\boxed{\sim e^{-\frac{q^2\langle \Delta r^2(t)\rangle}{6}}} \tag{7.1.7b}$$

where 'completing the square' is used to evaluate the integral. The result is precisely equation 2.3.5. So, equation 7.1.7b describes the electric field autocorrelation function (up to a constant) for Brownian motion of uniform spheres.

7.2 Stretched exponentials

The autocorrelation functions decay according to not just one relaxation process, but multiple, of varying characteristic relaxation times. Therefore, $g_2 - 1$ or g_1 can be expressed in terms of a sum of single exponential decays, each of different τ (or Γ), weighted by a distribution $G(\tau)$ which is a representation of the relative significance of one such decay.

$$g_1(t) \sim \int_0^\infty G(\tau)\exp\left[-(t/\tau)\right] d\tau \tag{7.2.1}$$

Under the assumption that $g_1(t) \sim \exp\left[-(t/\tau)^\beta\right]$, one can conclude that $\beta = 1$ corresponds to a single peak in the weighted distribution $G(\tau)$ and $\beta < 1$ corresponds to a broadening of $G(\tau)$. Thus, $\beta < 1$ is indicative of a superposition of many single-exponential decays in the correlation function, i.e.

$$g_1(t) \sim \exp\left[-(t/\tau)^\beta\right] = \int_0^\infty G(\tau)\exp\left[-(t/\tau)\right] d\tau \tag{7.2.2}$$

$G(\tau)$ can be found directly through Laplace inversion of g_1, although this is difficult with real correlation data, due to the degeneracy of solutions and noise. To calculate the average relaxation time, we must compute the area under g_1:

$$\int g_1(t)\mathrm{d}t \sim \int \exp\left[-(t/\tau)^\beta\right] dt \tag{7.2.3a}$$

$$= \frac{\tau}{\beta}\int e^{-u}\cdot u^{\left(\frac{1}{\beta}-1\right)} du \tag{7.2.3b}$$

$$= \frac{\tau}{\beta}\Gamma\left(\frac{1}{\beta}\right) \tag{7.2.3c}$$

where the substitution $u = (t/\tau)^{\beta}$, $\mathrm{d}t = \mathrm{d}u \cdot u^{\left(\frac{1}{\beta}-1\right)} \cdot \left(\frac{\tau}{\beta}\right)$ has been made. As the distribution is normalised to 1, the area is a direct representation of the average value of the horizontal axis, i.e. characteristic decay time. Therefore,

$$\boxed{\langle\tau\rangle = \frac{\tau}{\beta}\Gamma\left(\frac{1}{\beta}\right)} \tag{7.2.4}$$

7.3 The Siegert relation

The Siegert relation connects measurable ACFs, g_2, to unmeasurable ACFs, g_1. g_2 can be expressed as

$$g_2 = \frac{\langle I(t)\rangle \cdot \langle I(t+\tau)\rangle}{\langle I(t)\rangle^2} \tag{7.3.1}$$

where the intensities, $I(t)$ are defined by $I(t) = |E(t)|^2$ for electric fields $E(t)$. Considering the electric fields as wave functions with complex conjugate $E^*(t)$,

$$I(t) = \sum_{j,k} E_j(t) \cdot E_k^*(t) \tag{7.3.2}$$

summed over all indices j, k. g_2 can then be expressed as

$$g_2 = \frac{1}{\langle I(t)\rangle^2} \cdot \langle \sum_{j,k} E_j(t) \cdot E_k^*(t) \sum_{n,m} E_n(t+\tau) \cdot E_m^*(t+\tau)\rangle \tag{7.3.3}$$

When $j = k = n = m$, the summation gives $\langle I(t)\rangle^2$ and when $j = n, k = m$ but $j \neq k$, cross-terms of the form

$$\langle \sum_j I_j \cdot g_1(\tau) \sum_n I_n \cdot g_1^*(\tau)\rangle \tag{7.3.4}$$

appear. Therefore,

$$g_2 = \frac{\langle I(t)\rangle^2}{\langle I(t)\rangle^2} + \frac{\langle I(t)\rangle^2}{\langle I(t)\rangle^2} \cdot |g_1|^2 \tag{7.3.5a}$$

$$= 1 + |g_1|^2 \tag{7.3.5b}$$

$$\boxed{= 1 + \tilde{\beta}|g_1|^2} \tag{7.3.5c}$$

where the empirical factor $\tilde{\beta}$ is included as it is typically close but not exactly equal to 1.

7.4 Rouse, Zimm and reptation relaxation timescales

7.4.1 Rouse behaviour

Rouse behaviour is characterised by the lack of hydrodynamic interactions between polymer and solvent. The Rouse diffusion coefficient, D_R is related to characteristic length and time scales by $D_R \sim R^2/\tau_R$. The Stokes-Einstein relation assumes $D_R = \mu kT = kT/N\zeta$, where μ is the mobility of the chains, N is the number of chains, ζ is the friction factor *for one chain* and T is the solution temperature. The friction factor and

temperature do not depend on N nor on R, thus, $\tau_R \sim R^2/D_R \sim NR^2 \sim R^4$, using the fractal nature of polymers, $N \sim R^{d_f}$, and $d_f = 2$ for ideal chains. Thus, the characteristic time scale is $\boxed{\tau_R \sim R^4 \sim q^{-4}}$.

7.4.2 Zimm behaviour

The Zimm model considers hydrodynamic interactions for polymer chains in solution of hydrodynamic radius, R (the effective size in solution – a correlation length describing the range of hydrodynamic interactions). The Zimm diffusion coefficient, D_Z is related to R and a characteristic time scale through $D_Z \sim R^2/\tau_Z$. The Stokes-Einstein relation assumes $D_Z = \mu kT = kT/\zeta_{tot}$, although now the *total* friction factor, ζ_{tot}, is dependent on the effective size of the polymer chain in solution, R and independent of the number of monomers, N. So, $\tau_Z \sim R^2/D_Z \sim R \cdot R^2 \sim R^3 \Rightarrow \boxed{\tau_Z \sim q^{-3}}$.

7.4.3 Reptation behaviour

The reptation model is generally applicable for terminal time scales, towards the far end of the decay in the stress relaxation modulus, g_1 etc. The diffusion coefficient is $D_{rep} \sim L^2/\tau_{rep}$ where L^2 is proportional to the length of the reptation tube. L must be directly proportional to the number of monomers, N, that make up the tube and the Stokes-Einstein relation reads $D_{rep} = \mu kT = kT/N\zeta$, so $\tau_{rep} \sim L^2/D_{rep} \sim L^2 \cdot N \sim L^3$. Therefore, $\tau_{rep} \sim q^{-3}$. However, empirically it is found that $\tau_{rep} \sim q^{-3.4}$ due to the assumptions made in this model, such as L being assumed constant, when, in fact, L fluctuates constantly as chains diffuse.

7.5 Example raw data file

An example of a raw data file containing the raw $g_2 - 1$ vs t correlation data is shown below. Temperature, viscosity, refractive index, laser wavelength and angle are all given. The values given by “MeanCR0 [kHz]” and “MeanCR1 [kHz]” are the average intensities recorded by both detectors in the form of discrete photon counts, averaging to $\langle I \rangle_T$. For Pusey files, these values are averaged to give $\langle I \rangle_E$.

```
ALV-5000/E-WIN Data
Date : "1/7/2004"
Time : "12:17:07 PM"
Samplename : "PAAA 1wt% Sample 1"
SampMemo(0) :       "No beads, sample siting at RT since last measurement on "
SampMemo(1) :       "Nov. 17 2003"
SampMemo(2) :       ""
SampMemo(3) :       ""
SampMemo(4) :       ""
SampMemo(5) :       ""
SampMemo(6) :       ""
SampMemo(7) :       ""
SampMemo(8) :       ""
SampMemo(9) :       ""
Temperature [K] :        298.00317
Viscosity [cp]  :          0.89320
```

```
Refractive Index:          1.33200
Wavelength [nm] :        514.50000
Angle [°]       :         20.00000
Duration [s]    :         2700
Runs            :            1
Mode            :   "SINGLE CROSS CH0"
MeanCR0 [kHz]   :         65.19744
MeanCR1 [kHz]   :         96.27699

"Correlation"
*array of g2 − 1 vs t here*

"Count Rate"
*counts measured by each of the two detectors over the experiment time here*
```

7.6 Schematic of the ALV5000 spectrometer

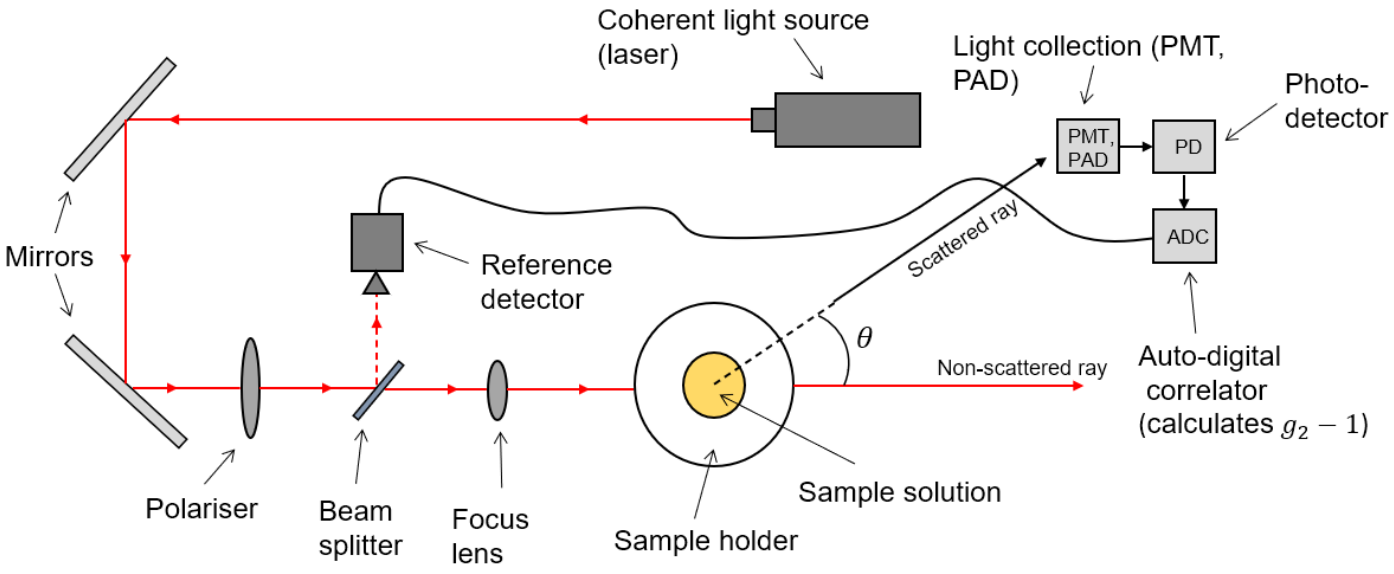

PMT: photomultiplier tube

PAD: pulse amplifier-discriminator

7.7 Definitions of variables, constants, functions etc

- k – usually written k_B, is the Boltzmann constant, equal to $1.38 \times 10^{-23}\ \mathrm{m^2 kgs^{-2} K^{-1}}$.
- T – temperature of the sample.
- kT – thermal energy: the energy associated with thermal fluctuations.
- p – site percolation occupation probability: the probability that any one lattice site becomes occupied.
- M – molecular mass of a polymer: the mass in grams per mole of polymer.

- R – a characteristic polymer chain size, may be the radius of the pervaded volume, the radius of gyration, the end-to-end distance etc.
- d_f – the fractal dimension, characterises the way an object fills space.
- τ (general) – characteristic structural relaxation time, the time taken for a decay to fall to $1/e$ times its peak height.
- n – the refractive index of solvent (water in this study), equal to the ratio of the speed of light in a vacuum to the speed of light in the medium ($c_\mathrm{medium} < c_0$).
- λ_0 – wavelength of the light emitted by the laser source.
- θ – the detector's angular position, variable between 20 and 140 degrees.
- q – the scattering wave vector, equal to the change in electromagnetic wave vector upon scattering. Expressed as $(4\pi n/\lambda_0)\sin(\theta/2)$. Measured in inverse microns, denoted $\mu\mathrm{m}^{-1}$. Note that this is not $10^{-6}\mathrm{m}^{-1}$, it is $10^{6}\mathrm{m}^{-1}$.
- t – lag time. The time delay between measurements of the intensity.
- $I(t)$ – the intensity measured as discrete counts at lag time t, equal to the magnitude of the electric field squared: $I(t) = |E(t)|^2$
- $\langle x \rangle$ – the average of a quantity, x. Can either be an ensemble average, taken across regions of a sample, or a temporal average, taken over time for one region.
- $g_2(t)$ – the time-dependent intensity autocorrelation function. A measure of the relationship between intensity measurements, closely associated with the relationship between sections of the sample. Equal to $(1/\langle I(t)\rangle^2) \cdot \langle I(0) \cdot I(t)\rangle$.
- $g_1(t)$ – the time-dependent electric field autocorrelation function. A measure of the relationship between intensity measurements, closely associated with the relationship between sections of the sample. Equal to $(1/\langle E(t)\rangle^2) \cdot \langle E(0) \cdot E(t)\rangle$
- $\langle \Delta r^2(t)\rangle$ – the time-dependent mean-squared displacement. Δr is the distance between the starting and ending points of a path taken by a diffusing particle.
- α – an empirical, fitting exponent used in power-law decays of g_1.
- $t^{-\alpha}$ – the power-law decay, for positive α.
- τ (stretched) – a fitting parameter, a characteristic relaxation time of the autocorrelation functions.
- β – stretching parameter, characterises the breadth of a decay. $\beta = 1$ represents a single exponential decay, while $\beta < 1$ is representative of a superposition of single exponentials.
- $e^{-(t/\tau)^\beta}$ – the stretched exponential decay.
- $\langle \tau \rangle$ – the average characteristic relaxation time of a stretched exponential decay. If $\beta = 1$ then $\langle \tau \rangle \equiv \tau$, but in general, $\langle \tau \rangle \neq \tau$. Equal to $(\tau/\beta) \cdot \Gamma(1/\beta)$ where Γ is the gamma function.
- $\Gamma(z)$ – the gamma function, equal to $\int_0^\infty e^{z-1}e^{-x}\mathrm{d}x$. Used as an extension of the factorial function, defined by $\Gamma(n) = (n-1)!$
- Γ – the decay rate of a relaxation process, equal to $1/\tau$.
- $\bar{\Gamma}$ – the average decay rate of a relaxation, equal to $1/\langle \tau \rangle$ and identical to Γ if $\beta = 1$.

- D – the diffusion coefficient, a constant relating the flux of diffusing particles to the driving force of diffusion. Equal to L^2/t for any suitable length and time scales L and t.
- Stokes-Einstein relation – derived from the Einstein relation, $D = kT/\zeta$ for friction factor ζ, and the Stokes relation, $\zeta = 6\pi\eta_s R$. Valid for uniform spheres travelling through a viscous medium for low Reynolds number flow (approximately laminar).
- η_s – viscosity of the solvent. In this study, the solvent is water, and its viscosity at room temperature is approximately $1 \times 10^{-3}\mathrm{pa} \cdot s$.
- η – viscosity of the sample, a sum of the viscosities of the solvent and the polymer.
- ξ (sol) – a correlation length, the average length over which parts of a sample remain correlated.
- ξ (gel) – an approximation of the mesh size of a gel, the average distance between cross-links.
- γ – an empirical exponent relating the average decay rate to the scattering wave vector, $\bar{\Gamma} = Dq^{\gamma}$ and $\gamma = 2$ for Brownian diffusion (random walks).
- $\tilde{\beta}$ – the coherence factor. An experimental parameter relating the size of the detector to the size of the region observed on the intensity pattern. Usually always less than 1. Used to relate g_1 to g_2 through the Siegert relation for ergodic systems, and the modified Siegert relation for non-ergodic systems.
- $\langle I \rangle_E$ – the average intensity measured over an ensemble. This can be measured over one sample via rotation (so all parts of the sample are seen) or over multiple identical samples.
- $\langle I \rangle_T$ – the average intensity measured over time.
- $Y = \langle I \rangle_E / \langle I \rangle_T$ – the ergodic ratio. Used in the modified Siegert relation for non-ergodic systems, to capture the dynamics of such a system more accurately.
- $\tilde{g}_2$ – the intensity autocorrelation function, normalised by the coherence factor.
- σ – the short-time intercept of $\tilde{g}_2 - 1$.
- c in wt% - the concentration, measured as the proportion of dissolved mass of polymer in solution, $= m_{\mathrm{polymer}}/m_{\mathrm{sample}}$.
- a – a constant used to scale autocorrelation data in a logarithmic plot with the aim of collapsing curves.
- l – an approximation of the probed length scale. Proportional to the inverse of the scattering wave vector, q^{-1}.
- l_c – a rough approximation of the critical probed length scale – the length scale at which the sample appears to switch between the gel and sol states. Proportional to ${q_c}^{-1}$.
- θ_c – a rough approximation of the detector angle at which the sample appears to switch between the gel and sol states. (i.e. g_1 decays to zero). Related to a critical wave vector, q_c.
- T_c – a critical temperature. Taken to be closely related to the sol-gel transition temperature in this study.
- VFT relation - $\langle \tau \rangle = \tau_0 \exp(A/(T - T_0))$.
- T_0 – the temperature at which the relaxation time diverges to infinity.
- τ_0 – a constant with units of time in the VFT expression. When $T \to \infty$, $\langle \tau \rangle \to \tau_0$, so this represents the relaxation time of the sol state.
- τ_1 – a constant with units of time in the critical temperature expression, $\langle \tau \rangle = \tau_1((T - T_c)/T_c)^{-\gamma}$ for positive γ. τ_1 is the timescale for relaxations when the temperature is $T = 2T_c$, well into the sol phase.